



Crane: Context-Guided Prompt Learning and Attention Refinement for Zero-Shot Anomaly Detections

Alireza Salehi^{1*}, Mohammadreza Salehi²,

Reshad Hosseini¹, Cees G. M. Snoek², Makoto Yamada³, Mohammad Sabokrou³

¹University of Tehran, ²University of Amsterdam, ³Okinawa Institute of Science and Technology

*Corresponding Author: alireza.salehy@ut.ac.ir

Abstract

Anomaly Detection (AD) involves identifying deviations from normal data distributions and is critical in fields such as medical diagnostics and industrial defect detection. Traditional AD methods typically require the availability of normal training samples; however, this assumption is not always feasible, as collecting such data can be impractical. Additionally, these methods often struggle to generalize across different domains. Recent advancements, such as AnomalyCLIP and AdaCLIP, utilize the zero-shot generalization capabilities of CLIP but still face a performance gap between image-level and pixel-level anomaly detection. To address this gap, we propose a novel approach that conditions the prompts of the text encoder based on image context extracted from the vision encoder. Also, to capture fine-grained variations more effectively, we have modified the CLIP vision encoder and altered the extraction of dense features. These changes ensure that the features retain richer spatial and structural information for both normal and anomalous prompts. Our method achieves state-of-the-art performance, improving performance by 2% to 29% across different metrics on 14 datasets. This demonstrates its effectiveness in both image-level and pixel-level anomaly detection. The code is available at <https://github.com/AlirezaSalehy/Crane>.

1. Introduction

Anomaly Detection involves learning the distribution of a given training dataset, which typically consists of normal samples—data that represents expected or typical behavior in a specific context—and identifying test samples that deviate from this learned distribution [50, 51]. Anomaly detection is useful in scenarios where anomalies are rare and difficult to collect but still necessary to detect. For instance, in medical diagnostics, datasets often contain an abundance of scans from healthy patients but very few from those with rare con-

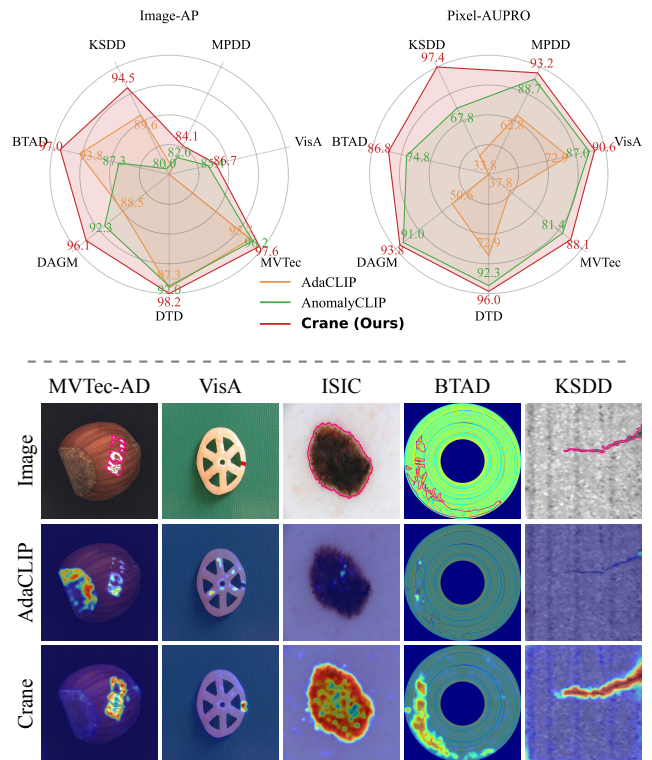


Figure 1. **Crane zero-shot anomaly detection performance compared to state-of-the-art.** The anomalous regions in each sample image are highlighted with pink outlines. As illustrated, Crane generates more precise localization maps and achieves superior image-level anomaly detection performance, as shown by the radar plots.

ditions [51]. Likewise, in industrial defect detection [38] and self-driving cars, normal data is more readily available, while anomalies such as manufacturing defects or unexpected road obstacles are rare but essential to identify [5]. In such cases, a dataset of frequently occurring (normal) samples is collected to train a model to detect abnormal ones.

Recent studies [7, 13, 26, 45, 66] indicate that obtaining normal data from all target domains is often impractical. To address this, zero-shot anomaly detection has been introduced, where models trained only on source data detect anomalies in unseen target datasets without requiring domain-specific training samples. Current methods either exploit CLIP’s [46] zero-shot capabilities through manually crafted textual prompts or adapt CLIP by learning prompts directly from source data, enabling generalization to new domains. Despite progress, generalization remains inconsistent at image-level versus pixel-level. For example, AdaCLIP [7] achieves state-of-the-art image-level results but shows limited pixel-level performance (50.2% AUPRO) on industrial benchmarks, highlighting challenges in precise anomaly localization, as shown by Figure 1.

We attribute this gap to two key challenges. First, abnormal regions are often small or share similar feature distributions with normal areas, making them difficult to distinguish. In previous works, these regions are typically identified by comparing the output of the text encoder for normal and abnormal prompts with the dense visual features. However, given the limited capacity of prompt learning, the text encoder often fails to generate representations that are discriminative enough to separate subtle anomalies from normal variations, leading to reduced segmentation accuracy. Second, while CLIP produces strong global representations, its dense features are not well-suited for segmentation tasks, limiting the model’s ability to capture fine details. AdaCLIP [7] attempts to address this by introducing trainable visual prompts, which enhance image-level classification. However, pixel-level anomaly detection remains challenging since dense visual features exhibit more variation than global representations, making it harder to capture fine-grained distinctions between normal and abnormal regions.

In this work, we propose `Crane` (Context-guided Prompt Learning and Attention Refinement) to address both challenges. To learn more discriminative prompts for the text encoder, we guide it using the image classification token (CLS) from the image encoder along with other learnable parameters, enabling it to generate outputs conditioned on the image context and improving the modeling of fine-grained distributions in a data-efficient manner. Additionally, we introduce a score-based pooling method to fuse global and dense feature knowledge in prompt learning, enhancing the modeling of abnormal region distributions. To better capture fine-grained variations, we modify the CLIP [46] vision encoder and extract dense features differently, ensuring they retain richer spatial and structural information for both normal and anomalous prompts. Finally, we propose a simple yet effective approach to integrate the knowledge of powerful vision encoders like DINOv2 [43]—despite their lack of inherent zero-shot compatibility—into the prompt learning process, further enhancing anomaly detection. We evaluate

`Crane` across 14 datasets from two domains—medical and industrial—demonstrating its effectiveness at both image and pixel levels. Our method consistently achieves high performance, improving state-of-the-art results with gains of 2% to 29% in anomaly detection and localization tasks.

2. Related Works

Unsupervised & Semi-supervised Anomaly Detection

Unsupervised and semi-supervised anomaly detection are dominantly used methods in the field; their main assumption is there is access to enough normal samples from the target domains. For unsupervised anomaly detection, a common strategy leverages pretrained models [38, 52] to extract discriminative features, modeling the normal distribution through mechanisms like knowledge distillation [2, 12, 53], memory banks [20, 47], reconstruction-based methods [17], and flow-based techniques [21, 61]. As the anomaly data is unavailable during training, some methods generate synthetic anomalies using self-supervised methods [39, 54], data augmentation [68], or generative models [9, 25, 40]. Some works directly use the diffusion models to better model normal data, resulting in better detection [18, 59, 63]. Semi-supervised anomaly detection methods incorporate a few anomalous samples during training [15, 44, 49, 60, 64] to cope with the lack of abnormal samples during training. Although effective, these methods assume the availability of enough normal samples from the target domain, differing from our objective. In contrast, we evaluate generalization performance on a target dataset while exclusively training on source data independent of that target, which is explained in the zero-shot anomaly detection.

Zero-shot anomaly detection Zero-shot anomaly detection methods assume no access to the target dataset; instead, they leverage foundation models [29, 33, 46], pretrained on large-scale datasets, to learn generalizable features from source data that can be applied to unseen target datasets. In particular, contrastive vision-language models, e.g., CLIP [46] which aligns global visual embeddings with textual descriptions. However, CLIP struggles with patch-level misalignment and lacks domain-specific sensitivity, limiting its ability to detect fine-grained anomalies. To address this issue, early methods focused on designing manually curated prompt templates [6, 10, 13, 26], which depend on domain knowledge and prompt quality. Whereas more recent works adopted prompt learning techniques [14, 48, 65] to automate prompt optimization in a few-shot setting. For instance, AnomalyCLIP [66] introduced object-agnostic prompts, simplifying prompt crafting while utilizing general anomalous patterns. To address the patch-level misalignment, some methods fine-tune the vision encoder [10, 10, 11, 34, 45, 67], keep the vision encoder frozen yet further refine its attention modules [35, 66], or

use deep token tuning in both text and vision encoder [7]. AnomalyCLIP [66] follows the second approach, which adds extra “VV” attention [36] to leverage patch embedding correlations, enhancing CLIP vision encoder segmentation ability. AdaCLIP [7] follows the latter approach by jointly tuning the vision and text encoders. It enhances feature alignment by introducing k-means clustering on dense visual features and adding learnable linear projection heads on the vision encoder. Although effective, our experiments reveal that AnomalyCLIP struggles with image-level generalization, whereas AdaCLIP underperforms at pixel-level detection. To address these shortcomings, we propose a context-guided prompt learning strategy to enhance alignment between textual and visual features and extend the attention refinement technique introduced by AnomalyCLIP. Unlike AdaCLIP, we do not fine-tune the vision encoder, as this can degrade its performance [62], and we avoid clustering techniques such as K-Means, which require additional hyperparameter tuning.

Problem Statement

Let M_θ denote a pretrained vision-language model (e.g., CLIP) with fixed parameters θ . We consider source anomaly detection datasets D_{train} from selected domains, where each image $x \in D_{\text{train}} \subset \mathbb{R}^{C \times H \times W}$ is paired with an image-level label

$$y \in \{0, 1\},$$

(with $y = 1$ indicating an anomaly and $y = 0$ a normal sample) and a pixel-level annotation

$$S \in \{0, 1\}^{H \times W},$$

with pixels labeled as 1 marking anomalous regions.

In zero-shot anomaly detection framework, given a prompt P the model produces two continuous anomaly scores for each image x :

$$\hat{y}, \hat{S} = M_\theta(x, P),$$

where $\hat{y} \in [0, 1]$ is the image-level anomaly score and $\hat{S} \in [0, 1]^{H \times W}$ is the pixel-level anomaly map. Here, P comprises textual templates (e.g., “a photo of normal CLS”) optionally augmented with learnable parameters, which are either prepended to or integrated within the textual input. The final image-level decision—classifying an image as normal or abnormal—is then obtained by thresholding \hat{y} as follows:

$$y' = \begin{cases} 1, & \text{if } \hat{y} > \tau, \\ 0, & \text{otherwise,} \end{cases}$$

where $y' = 1$ denotes an anomalous sample.

A common trend in zero-shot anomaly detection is to optimize the prompt P on D_{train} while keeping θ fixed, so

that P captures generalizable anomalous features. The optimized prompt P^* is then applied to new domains—where labeled anomaly data is unavailable—for both image- and pixel-level detection.

3. Method

We propose a unified framework that utilizes CLIP as a zero-shot backbone (M_θ) for classification and segmentation while adapting it for anomaly detection to bridge the domain gap between CLIP’s pretraining and specialized anomaly detection tasks. As shown in Figure 2, we learn class-agnostic input prompts (P) and trainable tokens inserted into the text encoder (Φ_t), guided by visual feedback from the vision encoder (Φ_v). To handle dense prediction, we adapt Φ_v by introducing the spatially aligned *E-Attn* branch, which enhances image-text alignment by refining CLIP’s attention, and the *D-Attn* branch, which integrates knowledge from a strong vision encoder such as DINOv2—despite its lack of inherent zero-shot compatibility—for finer-grained refinement. Finally, we introduce a score-based pooling mechanism that fuses anomalous dense features into the global image embedding, yielding more anomaly-aware global embedding enabling robust pixel- and image-level zero-shot generalization across previously unseen domains.

3.1. Local and Global Visual Feature Extraction

To craft the image anomaly score, \hat{y} , and the corresponding anomaly localization map, \hat{S} , in zero-shot, each input image needs to be modeled at both local (dense) and global (image-level) through our vision encoder Φ_v and then compared with the normal/abnormal text features extracted by the text encoder Φ_t . Each component is explained in detail below.

Adapted CLIP Vision Encoder (Φ_v). Given an input image x the vision encoder produces two outputs: a global embeddings $g_i \in \mathbb{R}^D$, used for classification, and local embeddings $Z^M \in \mathbb{R}^{2 \times N \times D}$ used for segmentation, where D denotes the dimension of embeddings and N Number of patch embeddings which are obtained from each of the *E-Attn* and *D-Attn* branches. The global representation g_i is the [CLS] token from the forward pass of the CLIP vision transformer, which extracts textually aligned image-level features. However, for local embeddings, we opt not to use the ViT’s original embeddings, as the emphasis on global image-text alignment during CLIP’s pretraining has led to degraded similarity between corresponding patch embeddings across layers, resulting in inaccurate segmentation [31, 36].

To address this, we adapt CLIP by replacing the Query-Key-based (QK^T) attention weighting with a self-correlation weighting scheme to reinforce semantic correlation across layers. Given $E \in \mathbb{R}^{N \times D}$ as a set of N embeddings, a self-correlation attention weighting can be defined

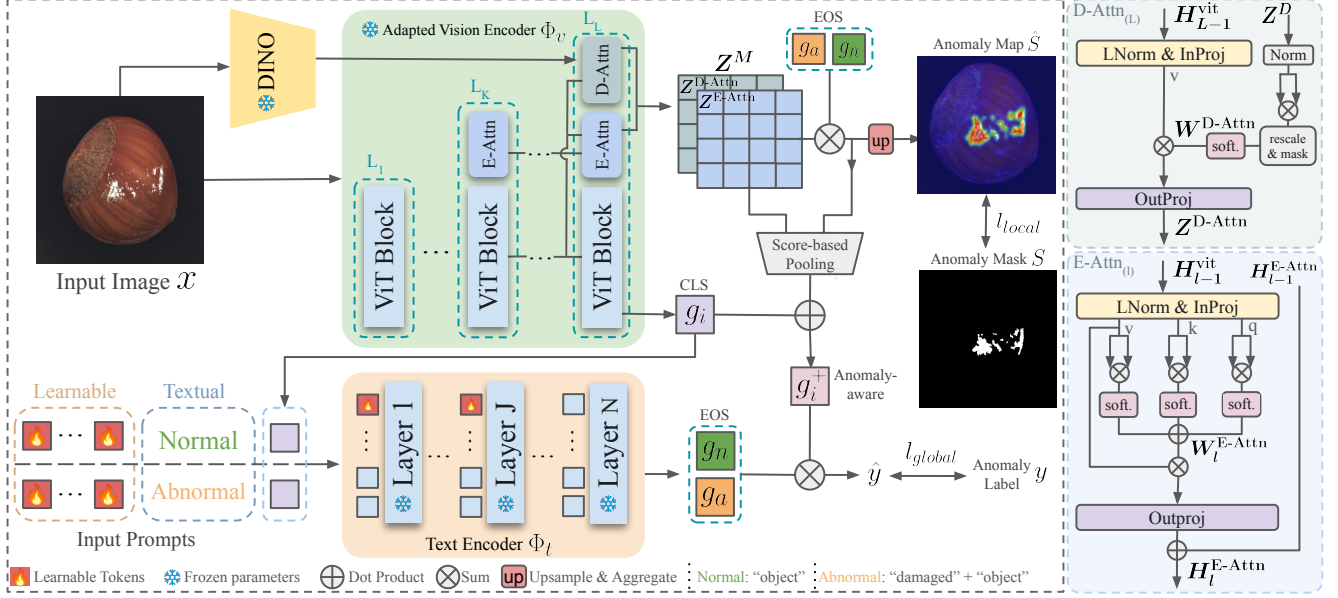


Figure 2. Crane framework for Zero-shot Anomaly Detection. First, we extract global embedding g_i and dual-branch spatially aligned local embeddings Z^{D-Attn} and Z^{E-Attn} by passing the image through the CLIP’s adapted vision encoder Φ_v . Next, we guide learnable prompts with global image context to enhance the capture of fine-grained anomalous patterns. We then compute anomaly map \hat{S} by measuring the similarity between visual embeddings and textual normal/anomalous embeddings. To boost image-level sensitivity to anomalies, we refine the global embedding by incorporating local embeddings weighted by their scores (g_i^+) and finally obtain anomaly score \hat{y} .

as:

$$A(E) = \text{softmax}\left(\frac{EE^\top}{\sqrt{D}}\right), \quad A(E) \in \mathbb{R}^{N \times N},$$

where $A(E)$ is a weight matrix that captures pairwise similarities between embeddings. We extend self-correlation weighting by applying the *Extended Self-Correlation Attention (E-Attn)* branch at layer l of CLIP ViT. Given $K_l, Q_l, V_l \in \mathbb{R}^{N \times D}$ as the *key*, *query*, and *value*, we compute attention weights as follows:

$$W_l^{E-Attn} = A(K_l) + A(Q_l) + A(V_l),$$

Then, the same as the standard attention [16], W_l^{E-Attn} is used to aggregate V_l tokens, producing H_l^{E-Attn} as the attention output. Since early layers have less expressive representations, this branch operates on the last K layers of the ViT. Given L as the total number of layers, for input image x the final output Z^{E-Attn} is obtained by aggregating intermediate outputs:

$$Z^{E-Attn} = \sum_{l=L-K+1}^L H_l^{E-Attn}, \quad Z^{E-Attn} \in \mathbb{R}^{N \times D}.$$

To assist CLIP with finer-grained alignment, we incorporate DINO [8, 42], which excels at capturing local representations but lacks inherent zero-shot capabilities. We

propose *DINO-guided spatial attention (D-Attn)*, which—like E-Attn—replaces original attention weights with more spatially aware ones. To achieve this, first we compute DINO’s patch similarities as follows:

$$Z^D = f_D(x), \quad S = \langle Z^D, Z^D \rangle,$$

where $Z^D \in \mathbb{R}^{N \times D}$ is DINO’s output patch embeddings, the operator $\langle \cdot, \cdot \rangle$ is cosine similarity and $S \in \mathbb{R}^{N \times N}$ is the computed similarity matrix. To refine S , we discard low similarity scores using a masking mechanism similar to ProxyCLIP [32] and apply softmax over the last dimension:

$$W^{D-Attn} = \text{softmax}(S + M), \quad M_{ij} = \begin{cases} 0, & S_{ij} \geq \epsilon, \\ -\infty, & S_{ij} < \epsilon, \end{cases}$$

The refined similarity matrix W^{D-Attn} is then used at layer l of CLIP’s ViT as attention weights for aggregating v_l embeddings, producing attention output $H_l^{D-Attn} \in \mathbb{R}^{N \times D}$. We apply D-Attn at the final layer L , making the branch output for x as:

$$Z^{D-Attn} = H_L^{D-Attn} \in \mathbb{R}^{N \times D}.$$

Text Encoder (Φ_t). To obtain the optimum textual alignment with anomalous visual embeddings, we employ prompt learning and deep token tuning within the text encoder. The standard transformer block $t_l(\cdot)$ at layer l is defined as:

$$[\text{SOS}_l, H_l, \text{EOS}_l] = t_l([\text{SOS}_{(l-1)}, H_{(l-1)}, \text{EOS}_{(l-1)}])$$

where $[\text{SOS}_l]$ and $[\text{EOS}_l]$ are special tokens marking the sequence’s start and end, and H_l represents intermediate token representations. For each layer $l = 2 \dots J + 1$, we replace the first M tokens of $H_{(l-1)}$ with learnable tokens $\tau_l \in \mathbb{R}^{M \times D}$ to capture anomaly-specific knowledge. At the final layer, the $[\text{EOS}]$ token, which aggregates the semantic representation of the input prompt, is used as the textual feature.

To design the input prompt, we abandon class-based, manually crafted templates in favor of object-agnostic learnable prompts [66]. As a result, we learn only two prompts (normal and anomalous), instead of two per dataset category. This approach leverages the shared structural patterns of anomalies across domains and reduces the need for domain-specific prompt engineering. To achieve this, we use a set of E learnable tokens for each of the normal and anomalous prompts, denoted by $\tau^n, \tau^a \in \mathbb{R}^{E \times D}$, and concatenate them with general product and state textual descriptions: “object” for the normal case and “damaged object” for the anomalous case, appended after the learnable sets.

Additionally, we introduce *context-guided prompt learning*, which integrates the image-level representation g_i into textual prompts during training, enabling the model to better capture fine-grained distributions. In summary, the normal g_n and abnormal textual embedding g_a are constructed as:

$$g_n = T([\tau_1^n, \tau_2^n, \dots, \tau_E^n, \text{“object”}, g_i]),$$

$$g_a = T([\tau_1^a, \tau_2^a, \dots, \tau_E^a, \text{“damaged”}, \text{“object”}, g_i]).$$

Calculating anomaly likelihood. Having obtained the textual $G = \{g_n, g_a\}$ and visual embeddings $e \in \{g_i, Z_{j,k}\}$, where $Z_{j,k}$ represents patch embedding at the position (j, k) of unflattened local feature branch $Z \in Z^M = \{Z^{\text{D-Attn}}, Z^{\text{E-Attn}}\}$ for input image x , we can now compute the likelihood of each visual embedding belonging to the anomalous class (p_a) by applying the Softmax function to similarity scores:

$$p_a(e, G) = \frac{\exp(\langle e, g_a \rangle / \tau)}{\exp(\langle e, g_a \rangle / \tau) + \exp(\langle e, g_n \rangle / \tau)} \quad (1)$$

where the temperature τ is set to 100 according to CLIP’s hyperparameter details [46]. We denote the probability of a visual embedding e being abnormal, $p_a(e, G)$, as its anomaly score.

3.2. Anomaly-aware Global Tuning through Local Fusion

The image-level representation g_i , trained to capture a global representation of an image, may fail to encode the discriminative fine-grained anomalous cues due to its global focus. To address this issue, we propose a *score-based spatial pooling* mechanism that fuses patch-level features into g_i based

on their anomaly scores, ensuring the final representation preserves global semantics while capturing anomaly cues. For each local feature map $Z \in \mathbb{R}^{H \times W \times D}$ from Z^M , The anomaly-aware representation is constructed as:

$$g_a^z = \frac{\sum_{j,k} p_a(Z_{j,k}, G) Z_{j,k}}{\sum_{j,k} p_a(Z_{j,k}, G)}, \quad Z \in \{Z^{\text{D-Attn}}, Z^{\text{E-Attn}}\}.$$

After obtaining $g_a^{\text{D-Attn}}$ and $g_a^{\text{E-Attn}}$ for each branch, we fuse these anomaly-aware embeddings into g_i via averaging:

$$\bar{g}_a = \frac{g_a^{\text{E-Attn}} + g_a^{\text{D-Attn}}}{2}, \quad g_i^+ = \frac{g_i + \bar{g}_a}{2},$$

where g_i^+ is the anomaly-aware global representation used for anomaly classification.

3.3. Training

To train the text encoder Φ_t , we employ global and local loss functions. For input image x the global loss ensures alignment between the global embedding g_i^+ and its corresponding textual embedding (g_a and g_n) being learned using Binary Cross Entropy and image-level label y :

$$L_{\text{global}} = \text{BCE}(y, p_a(g_i, G)).$$

For local loss, we use Focal [37] and Dice [55] loss at pixel-level. For output feature map $Z \in Z^M$, we compute normal and anomaly maps S_n^Z and S_a^Z based on the equation 1, then apply bilinear upsampling $\text{Up}(\cdot)$ to match the anomaly mask $S \in \mathbb{R}^{H \times W}$:

$$L_{\text{local}}^Z = \text{Focal}(\text{Up}([S_n^Z, S_a^Z]), S) + \text{Dice}(\text{Up}([S_n^Z, S_a^Z]), S).$$

Finally, we combine both terms using λ as a weighting factor controlling the contribution of the local loss.

$$L_{\text{total}} = L_{\text{global}} + \lambda \sum_{Z \in Z^M} L_{\text{local}}^Z.$$

4. Inference

For each input image x , after computing visual outputs including local features $Z \in Z^M$ and anomaly-aware global embedding g_i^+ alongside textual embeddings $G = \{g_a, g_n\}$ in forward pass, anomaly score \hat{y} and low-resolution anomaly maps \hat{S}_a^Z is calculated as follows:

$$\hat{y} = p_a(g_i^+, G), \quad \hat{S}_{a,(j,k)}^Z = p_a(Z_{j,k}, G),$$

where $\hat{S}_{a,(j,k)}^Z$ is anomaly score for each patch at location (j, k) . We then perform averaging on $\hat{S}_a^{\text{D-Attn}}$ and $\hat{S}_a^{\text{E-Attn}}$, then apply bilinear upsampling and Gaussian filter smoothing to obtain final anomaly maps \hat{S} .

5. Experiments

5.1. Experiments Setting

Datasets. To ensure a comprehensive evaluation, we conduct experiments on 14 real-world anomaly detection datasets spanning industrial defect detection and medical abnormality analysis across diverse domains and anomaly types. For industrial anomaly detection, we utilize MVTec AD [3], VisA [68], DTD-Synthetic [1], SDD [56], BTAD [41], DAGM [58], and MPDD [27], which primarily focus on texture and structural defects in manufactured scenarios. For medical anomaly detection, we evaluate on ISIC [22], CVC-ColonDB [57], CVC-ClinicDB [4], TN3K [19], BrainMRI [28], HeadCT [30], and BR35H [23], covering pathological abnormalities across dermoscopic, colonoscopic, retinal, and brain imaging domains. Following prior works [7, 66], for all experiments, we train our model on MVTec AD and evaluate its generalization to other datasets. To assess performance on MVTec itself, we use VisA, which contains non-overlapping sample categories. Further details on preprocessing and hyperparameters are provided in Appendix A.

Evaluation Metrics. Following previous studies [10, 13, 26], we employ AUROC, AP, and F1-max to evaluate the model’s ability to distinguish between normal and anomalous images. For pixel-level anomaly localization, we use AUROC, AUPRO, and F1-max to assess effectiveness in identifying anomalous regions. For each dataset, we report the average performance across object categories as the dataset-level result.

5.2. Main Results

Baselines. We compare our method against two categories of CLIP-based zero-shot anomaly detection (ZSAD) approaches: training-free and training-required methods. Training-free methods do not require auxiliary dataset training, or any additional supervision, including AnoVL [13] and WinCLIP [26]. Training-required methods involve training on an auxiliary dataset before inference, such as VAND [10], AnomalyCLIP [66], and AdaCLIP [7]. Details on the reported metrics, either sourced from the respective papers or reproduced if unavailable, are provided in Appendix B.

Zero-shot Performance over Industrial Datasets. We evaluate and compare the generalization of *Crane* on seven industrial datasets in Table 1. We show the performance of our method with and without D-Attn modules for a fair comparison. As shown, our method with or without using D-Attn module sets a new state-of-the-art in both image and pixel-level tasks. In image-level, we improve AUROC by 2.3%, AP by 4.3%, and F1-max by 0.5%, showing a considerably better global understanding of input images compared to

other methods. This improvement stems from learning normal and anomaly prompts that are more effectively aligned with visual tokens by providing additional context to the text encoder. Furthermore, by incorporating dense feature information into the global representation through score-based pooling, our approach encourages a more precise classification boundary, reducing reliance on spurious correlations that can arise when using only global representations. This is particularly evident in the improved AP and F1-max scores.

Our pixel-level improvements surpass even those at the image level, achieving 2.4% higher AUROC, 9% higher AUPRO, and a 3.8% increase in F1-max, significantly outperforming the previous state-of-the-art. The improvement can be attributed to the modifications applied to CLIP vision transformer via E-Attn modules, which extract more expressive dense features for both normal and anomalous samples. Particularly, in detecting smaller regions—reflected in the higher AUPRO scores—*Crane* surpasses AdaCLIP, the state-of-the-art in image-level classification, by approximately 49% without using D-Attn modules. When E-Attn and D-Attn modules are combined, the gap extends beyond 52%, demonstrating our method’s strong capability in tackling challenging segmentation tasks.

Zero-shot Generalization to Medical Domain. Here, we assess how well the features learned on industrial datasets generalize to domains far from the industrial domain. To this end, we evaluate *Crane* on seven medical datasets spanning diverse applications, including skin cancer detection in photography images, colon polyp identification in endoscopy images, thyroid nodule detection in ultrasound images, and brain tumor detection in MRI images. The goal is to determine whether the model has developed a broader understanding of normality and abnormality.

Table 2 presents the results, showing that *Crane* consistently outperforms existing methods, achieving a 3.0% increase in image-level AUROC and a 3.6% boost in AP. At the pixel level, it improves AUPRO by 5.0% and F1-max by 2.3%, demonstrating strong zero-shot generalization across challenging medical datasets. Additionally, our variant without D-Attn modules achieves results very close to the full model in classification tasks, outperforming all other models and remaining competitive with AnomalyCLIP in segmentation. This indicates that the primary contribution of the DINO-based attention lies in enhancing segmentation performance and improving out-of-domain generalization.

5.3. Ablation Study

To assess the effectiveness of each contribution, we conduct a series of controlled ablation experiments. All models are trained for five epochs, with only a single component modified at each stage while keeping all other factors unchanged. We report F1-max and AUROC scores on VisA and MVTec-

Table 1. **Comparison of ZSAD methods in the industrial domain.** We compare our method against the current state-of-the-art across seven diverse industrial datasets. The best performance is highlighted in **bold**, while the second-best is underlined. A [†] symbol next to a method name indicates training-free models. Unlike AnomalyCLIP and AdaCLIP, which fail to achieve consistent improvements, both versions of our model enhance the state-of-the-art in image-level and pixel-level metrics. Higher values indicate improved performance.

Metric	Dataset	WinCLIP [†] [26]	AnoVL [†] [13]	VAND [10]	AnomalyCLIP [66]	AdaCLIP [7]	Ours w/o D-Attn	Ours
Image-level (AUROC, AP, F1-max)	MVTec	(91.8, 96.5, 92.9)	(92.5, 95.1, 93.2)	(86.1, 93.5, 88.9)	(91.5, 96.2, 92.7)	(89.2, 95.7, 90.6)	(93.8, 97.5, 93.8)	(93.9, 97.6, 93.6)
	VisA	(78.1, 81.1, 80.7)	(79.2, 80.2, 79.7)	(78.0, 81.4, 80.7)	(82.1, 85.4, 80.4)	(85.8, 79.0, 83.1)	(85.3, 87.9, 82.6)	(83.6, 86.7, 81.2)
	MPDD	(63.6, 69.9, 77.5)	(72.7, 83.6, 88.3)	(73.0, 80.2, 76.0)	(77.0, 82.0, 80.4)	(76.0, 80.2, 82.5)	(81.4, 84.8, 81.6)	(81.0, 84.1, 83.0)
	BTAD	(68.2, 70.9, 67.6)	(80.3, 72.8, 73.0)	(73.6, 68.6, 82.0)	(88.3, 87.3, 83.8)	(88.6, 93.8, 88.2)	(94.4, 95.9, 91.7)	(96.3, 97.0, 93.7)
	KSDD	(84.3, 77.4, 79.0)	(94.4, 90.8, 88.0)	(79.8, 71.4, 85.2)	(84.7, 80.0, 82.7)	(97.1, 89.6, 90.7)	(97.8, 94.3, 91.6)	(97.8, 94.5, 89.7)
	DAGM	(91.8, 79.5, 87.6)	(89.7, 76.1, 74.7)	(94.4, 83.8, 91.8)	(97.5, 92.3, 90.1)	(99.1, 88.5, 97.5)	(99.2, 97.4, 95.8)	(98.9, 96.1, 94.7)
	DTD	(93.2, 92.6, 94.1)	(94.9, 93.3, 97.3)	(94.6, 95.0, 96.8)	(93.5, 97.0, 93.6)	(95.5, 97.3, 94.7)	(96.3, 98.5, 95.3)	(95.8, 98.2, 94.6)
Average	(81.6, 81.1, 82.8)	(86.2, 84.6, 84.9)	(81.6, 82.0, 85.9)	(87.8, 88.6, 87.2)	(90.2, 89.2, 89.6)	(92.6, 93.7, 90.3)	(92.5, 93.5, 90.1)	
Pixel-level (AUROC, AUPRO, F1-max)	MVTec	(85.1, 64.6, 31.6)	(90.6, 77.8, 36.5)	(87.6, 44.0, 39.8)	(91.1, 81.4, 39.1)	(88.7, 37.8, 43.4)	(91.3, 84.6, 41.3)	(91.2, 88.1, 43.8)
	VisA	(79.6, 56.8, 14.8)	(85.2, 60.5, 14.6)	(85.2, 86.8, 32.3)	(95.5, 87.0, 28.3)	(95.5, 72.9, 37.7)	(95.1, 87.5, 30.9)	(95.3, 90.6, 30.2)
	MPDD	(76.4, 48.9, 15.4)	(62.3, 38.3, 15.6)	(94.1, 83.2, 30.6)	(96.5, 88.7, 34.2)	(96.1, 62.8, 34.9)	(97.0, 89.3, 38.2)	(97.6, 93.2, 42.0)
	BTAD	(72.7, 27.3, 18.5)	(75.2, 40.9, 23.4)	(60.8, 25.0, 38.4)	(94.2, 74.8, 49.7)	(92.1, 20.3, 51.7)	(96.6, 81.3, 56.9)	(96.7, 86.8, 61.1)
	KSDD	(68.8, 24.2, 21.3)	(97.1, 82.6, 23.1)	(79.8, 65.1, 56.2)	(90.6, 67.8, 51.3)	(97.7, 33.8, 54.5)	(97.9, 95.9, 60.2)	(99.2, 97.4, 62.4)
	DAGM	(87.6, 65.7, 13.9)	(79.7, 56.0, 12.8)	(82.4, 66.2, 57.9)	(95.6, 91.0, 58.9)	(91.5, 50.6, 57.5)	(96.3, 91.2, 67.2)	(96.2, 93.8, 66.8)
	DTD	(83.9, 57.8, 16.1)	(97.7, 90.5, 46.8)	(95.3, 86.9, 72.7)	(97.9, 92.3, 62.2)	(97.9, 72.9, 71.6)	(98.3, 93.3, 68.8)	(98.8, 96.0, 71.8)
Average	(79.2, 49.3, 18.8)	(84.0, 63.8, 24.7)	(84.9, 65.3, 46.8)	(94.5, 83.3, 46.2)	(94.2, 50.1, 50.2)	(96.1, 89.0, 51.9)	(96.4, 92.3, 54.0)	

Table 2. **Comparison of ZSAD methods in the medical domain.** To further evaluate our model’s generalization, we assess its performance across diverse medical datasets. The best performance is highlighted in **bold**, while the second-best is underlined. A [†] symbol next to a method name indicates training-free models. Our method achieves competitive performance or significant improvement compared to the state-of-the-art as shown by image and pixel metrics. Higher values indicate improved performance.

Metric	Dataset	WinCLIP [†] [26]	AnoVL [†] [13]	VAND[10]	AnomalyCLIP[66]	AdaCLIP[7]	Ours w/o D-Attn	Ours
Image-level (AUROC, AP, F1-max)	HeadCT	(81.8, 80.2, 79.8)	(82.3, 81.2, 79.1)	(89.2, 89.5, 82.1)	(93.4, 91.6, 90.8)	(91.8, 90.6, 84.1)	(95.3, 95.7, 91.1)	(94.6, 95.4, 89.7)
	BrainMRI	(86.6, 91.5, 86.3)	(84.3, 89.2, 84.8)	(89.6, 91.0, 88.5)	(90.3, 92.2, 90.2)	(93.5, 95.6, 89.7)	(95.4, 96.1, 93.9)	(96.3, 97.4, 93.5)
	Br35H	(80.5, 82.2, 74.4)	(80.0, 80.7, 75.2)	(91.4, 91.9, 84.2)	(94.6, 94.7, 89.1)	(92.3, 93.2, 85.3)	(96.3, 96.8, 91.7)	(96.4, 97.2, 91.0)
	Average	(83.0, 84.6, 80.2)	(82.2, 83.7, 79.7)	(90.1, 90.8, 84.9)	(92.8, 92.8, 90.0)	(92.5, 93.1, 86.4)	(95.7, 96.2, 92.2)	(95.8, 96.7, 91.4)
Pixel-level (AUROC, AUPRO, F1-max)	ISIC	(83.3, 55.1, 48.5)	(92.6, 82.2, 76.6)	(89.5, 77.8, 71.5)	(89.7, 78.4, 70.6)	(90.3, 54.7, 72.6)	(88.1, 75.3, 69.8)	(90.6, 83.2, 73.4)
	ColonDB	(70.3, 32.5, 19.6)	(76.2, 44.1, 26.8)	(78.4, 64.6, 29.7)	(81.9, 71.3, 37.3)	(82.6, 66.0, 36.1)	(82.5, 73.0, 36.0)	(86.0, 78.6, 40.2)
	ClinicDB	(51.2, 13.8, 24.4)	(79.7, 51.4, 36.3)	(80.5, 60.7, 38.7)	(82.9, 67.8, 42.1)	(82.8, 66.4, 40.9)	(84.0, 69.3, 42.5)	(88.3, 74.5, 47.9)
	TN3K	(70.7, 39.8, 30.0)	(70.2, 34.4, 32.3)	(73.6, 37.8, 35.6)	(81.5, 50.4, 47.9)	(76.8, 34.0, 40.7)	(79.4, 48.8, 44.7)	(80.4, 51.7, 45.5)
	Average	(68.9, 35.3, 30.6)	(79.7, 53.0, 43.0)	(80.5, 60.2, 43.9)	(84.0, 67.0, 49.5)	(83.1, 55.3, 47.6)	(83.5, 66.6, 48.2)	(86.4, 72.0, 51.8)

AD for both image- and pixel-level performance.

Score-Based Dense Feature Pooling. As shown in Table 3.a, aggregating anomalous local embeddings into the global [CLS] token improves F1-max by 1.9% on average, demonstrating the effectiveness of anomaly-aware global refinement. This gain stems from the global token’s limited capacity to capture fine-grained anomalous patterns. Score-based dense feature pooling, as a parameter-free attention mechanism, sharpens the model’s focus on anomaly-relevant regions.

Context-guided Prompt Learning. To assess the impact of context-guided prompt learning, we compare model performance with and without concatenating g_i (the visual [CLS] token) to the input prompts. As shown in Table 3.b, incorporating train-domain representations during training consistently enhances both pixel-level and image-level performance across VisA and MVTEC-AD datasets. On average,

F1-max increases by 0.9% across both performance levels. This improvement can be attributed to the ability to better model fine-grained anomalous patterns given the global context of train images.

Attention Refinement. In Table 3.c the effect of using separate attention tokens (qq , kk , or vv) and their combinations ($qq + kk$ or $qq + kk + vv$) for self-correlation attention is examined. Extending self-correlation to include all three tokens ($qq + kk + vv$) improves pixel-level F1-max by 1.7% and image-level F1-max by 0.5% over the vv -only baseline. These results suggest that qq , kk , and vv capture certain spatial information exclusively, therefore combining them improves alignment.

Attention Ensembling. Table 3.d investigates the effectiveness of the spatially refined branches: E-Attn (first row) and D-Attn (second and third rows), used independently or in combination (fourth row). For D-Attn, we also compare dif-

Table 3. **Ablation analysis of key components.** Performance is reported at image-level (I-ROC, I-F1-max) and pixel-level (P-ROC, P-F1-max) on MVTec-AD and VisA. Higher values indicate improved performance. Colored rows denote the default configuration.

(a) Effect of Score-based dense feature pooling.					(b) Effect of context-guided Prompt Learning.				
Score	Image-level				Train	Pixel-level		Image-level	
	MVAD	VisA	MVAD	VisA		MVAD	VisA	MVAD	VisA
✗	(90.7, 92.3)	(79.2, 78.9)			✗	(91.7, 43.5)	(94.8, 28.1)	(94.0, 93.3)	(81.9, 80.2)
✓	(94.7, 94.3)	(82.6, 80.6)			✓	(92.1, 44.7)	(95.5, 29.2)	(94.7, 94.3)	(82.6, 80.6)

(c) Effect of different self-correlations for E-Attn.					(d) Effect of spatial branches. Superscripts 1, 2, and 3 refer to the specific models used: (1) CLIP-B14, (2) DINOv1-B8, (3) DINOv2-B14.				
Self-cors.	Pixel-level		Image-level		Branch	Pixel-level		Image-level	
	MVAD	VisA	MVAD	VisA		MVAD	VisA	MVAD	VisA
kk	(91.6, 43.5)	(94.9, 27.9)	(93.6, 93.7)	(82.2, 80.4)	E-Attn ¹	(91.2, 40.8)	(94.3, 29.5)	(93.7, 93.9)	(82.7, 80.4)
vv	(92.1, 43.8)	(95.0, 26.7)	(93.8, 93.3)	(82.4, 80.7)	D-Attn ²	(91.5, 43.7)	(94.0, 27.1)	(91.1, 92.9)	(78.4, 78.9)
qq	(91.8, 43.9)	(95.0, 29.4)	(94.1, 94.0)	(80.2, 79.4)	D-Attn ³	(92.0, 42.7)	(93.7, 26.7)	(91.6, 92.6)	(78.3, 78.3)
qq+kk	(91.6, 44.0)	(95.2, 29.3)	(94.0, 93.9)	(82.3, 80.5)	Both ¹⁺³	(92.1, 44.7)	(95.5, 29.2)	(94.7, 94.3)	(82.6, 80.6)
qq+kk+vv	(92.4, 44.7)	(95.5, 29.2)	(94.7, 94.3)	(82.6, 80.6)					

ferent variants of DINO. Our adapted CLIP model (first row) outperforms D-Attn (second and third rows) in image classification by a significant margin. Combining both DINO and CLIP (fourth row) yields the best results, improving pixel-level F1-max by 1.8% and image-level F1-max by 0.3% on average compared to using CLIP alone. This improvement highlights the complementary strengths of the two branches: D-Attn excels at capturing visual similarity across patches but lacks semantic sensitivity, whereas E-Attn better preserves semantic information but struggles with fine-grained alignment.

5.4. Visual Analysis

To gain an intuitive comparison, we provide anomaly maps generated by the top competing models—VAND, AdaCLIP, AnomalyCLIP—and *Crane*, across a diverse set of images from MVTec-AD, VisA, MPDD, BTAD, DAGM, and DTD-Synthetic. AdaCLIP and VAND struggle to maintain a balance between true positive and false negative rates. AnomalyCLIP further enhances sensitivity but continues to exhibit a high false negative rate, limiting its effectiveness. In contrast, *Crane* benefits from a stronger semantic correlation among patches, which improves the true positive rate while reducing false positives simultaneously, demonstrating its superior localization performance. Further quantitative and qualitative comparisons are provided in the Appendix D.

6. Conclusion

In this study, we introduced *Crane* for zero-shot anomaly detection. Our approach enhanced CLIP’s patch-level alignment through a dual-branch, spatially aware attention weight-

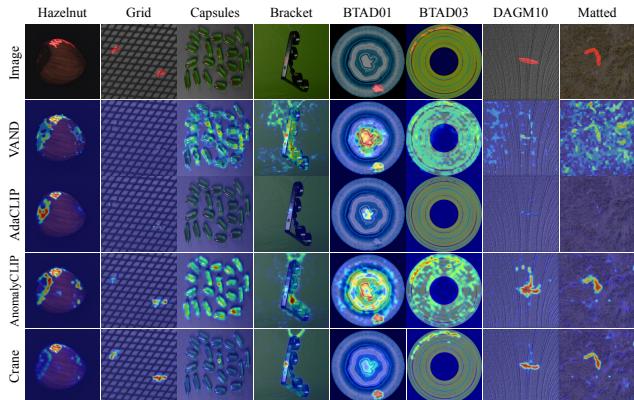


Figure 3. **Qualitative localizations.** The anomaly regions are painted in red in each sample image. *Crane* achieves more precise and consistent anomaly localization across diverse objects and textures compared to prior methods.

ing refinements, leveraging self-correlation of attention tokens and the strong spatial alignment of DINO’s patch embeddings. Additionally, we increased image-level sensitivity to anomalous regions with a local-to-global fusion and improved modeling fine-grained anomalous patterns, leveraging visual context in prompt learning. Extensive experiments across 14 datasets spanning medical and industrial domains demonstrated that *Crane* achieves state-of-the-art performance in zero-shot anomaly detection and localization. *Limitations.* Despite *Crane*’s strong performance and generalization capabilities, a performance gap persists compared to unsupervised methods that assume access to normal training samples and leverage full-shot training pipelines. This gap

partly stems from the inherent challenge zero-shot models face in detecting unseen semantic anomalies, where domain knowledge is crucial to distinguish normal from anomalous samples. Figure 17 (Appendix) illustrates this challenge: for instance, the blue tube is not flagged as anomalous because it lacks general structural defects, yet it is semantically inconsistent within the local context of the dataset.

Acknowledgements

Mohammad Sabokrou’s work in this project was supported by JSPS KAKENHI Grant Number 24K20806.

References

- [1] Toshimichi Aota, Lloyd Teh Tzer Tong, and Takayuki Okatani. Zero-shot versus many-shot: Unsupervised texture anomaly detection. In *Proceedings of the IEEE/CVF Winter Conference on Applications of Computer Vision*, pages 5564–5572, 2023.
- [2] Kilian Batzner, Lars Heckler, and Rebecca König. Efficientad: Accurate visual anomaly detection at millisecond-level latencies. In *Proceedings of the IEEE/CVF Winter Conference on Applications of Computer Vision*, pages 128–138, 2024.
- [3] Paul Bergmann, Michael Fauser, David Sattlegger, and Carsten Steger. Mvtec ad—a comprehensive real-world dataset for unsupervised anomaly detection. In *Proceedings of the IEEE/CVF conference on computer vision and pattern recognition*, pages 9592–9600, 2019.
- [4] Jorge Bernal, F Javier Sánchez, Gloria Fernández-Esparrach, Debora Gil, Cristina Rodríguez, and Fernando Vilariño. Wm-dova maps for accurate polyp highlighting in colonoscopy: Validation vs. saliency maps from physicians. *Computerized medical imaging and graphics*, 43:99–111, 2015.
- [5] Daniel Bogdoll, Maximilian Nitsche, and J Marius Zöllner. Anomaly detection in autonomous driving: A survey. In *Proceedings of the IEEE/CVF conference on computer vision and pattern recognition*, pages 4488–4499, 2022.
- [6] Yunkang Cao, Xiaohao Xu, Chen Sun, Yuqi Cheng, Zongwei Du, Liang Gao, and Weiming Shen. Segment any anomaly without training via hybrid prompt regularization. *arXiv preprint arXiv:2305.10724*, 2023.
- [7] Yunkang Cao, Jiangning Zhang, Luca Frittoli, Yuqi Cheng, Weiming Shen, and Giacomo Boracchi. Adaclip: Adapting clip with hybrid learnable prompts for zero-shot anomaly detection. In *European Conference on Computer Vision*, pages 55–72. Springer, 2024.
- [8] Mathilde Caron, Hugo Touvron, Ishan Misra, Hervé Jégou, Julien Mairal, Piotr Bojanowski, and Armand Joulin. Emerging properties in self-supervised vision transformers. In *Proceedings of the IEEE/CVF international conference on computer vision*, pages 9650–9660, 2021.
- [9] Qiyu Chen, Huiyuan Luo, Chengkan Lv, and Zhengtao Zhang. A unified anomaly synthesis strategy with gradient ascent for industrial anomaly detection and localization. In *European Conference on Computer Vision*, pages 37–54. Springer, 2024.
- [10] Xuhai Chen, Yue Han, and Jiangning Zhang. April-gan: A zero-/few-shot anomaly classification and segmentation method for cvpr 2023 vand workshop challenge tracks 1&2: 1st place on zero-shot ad and 4th place on few-shot ad. *arXiv preprint arXiv:2305.17382*, 2023.
- [11] Xuhai Chen, Jiangning Zhang, Guanzhong Tian, Haoyang He, Wuhao Zhang, Yabiao Wang, Chengjie Wang, and Yong Liu. Clip-ad: A language-guided staged dual-path model for zero-shot anomaly detection. In *International Joint Conference on Artificial Intelligence*, pages 17–33. Springer, 2024.
- [12] Hanqiu Deng and Xingyu Li. Anomaly detection via reverse distillation from one-class embedding. In *Proceedings of the IEEE/CVF conference on computer vision and pattern recognition*, pages 9737–9746, 2022.
- [13] Hanqiu Deng, Zhaoxiang Zhang, Jinan Bao, and Xingyu Li. Anovl: Adapting vision-language models for unified zero-shot anomaly localization. *arXiv preprint arXiv:2308.15939*, 2023.
- [14] Mohammad Mahdi Derakhshani, Enrique Sanchez, Adrian Bulat, Victor G. Turrissi da Costa, Cees G.M. Snoek, Georgios Tzimiropoulos, and Brais Martinez. Bayesian prompt learning for image-language model generalization. In *Proceedings of the IEEE/CVF International Conference on Computer Vision (ICCV)*, pages 15237–15246, 2023.
- [15] Choubao Ding, Guansong Pang, and Chunhua Shen. Catching both gray and black swans: Open-set supervised anomaly detection. In *Proceedings of the IEEE/CVF conference on computer vision and pattern recognition*, pages 7388–7398, 2022.
- [16] Alexey Dosovitskiy, Lucas Beyer, Alexander Kolesnikov, Dirk Weissenborn, Xiaohua Zhai, Thomas Unterthiner, Mostafa Dehghani, Matthias Minderer, Georg Heigold, Sylvain Gelly, et al. An image is worth 16x16 words: Transformers for image recognition at scale. *arXiv preprint arXiv:2010.11929*, 2020.
- [17] Zheng Fang, Xiaoyang Wang, Haocheng Li, Jiejie Liu, Qiugui Hu, and Jimin Xiao. Fastrecon: Few-shot industrial anomaly detection via fast feature reconstruction. In *Proceedings of the IEEE/CVF International Conference on Computer Vision*, pages 17481–17490, 2023.
- [18] Matic Fučka, Vitjan Zavrtnik, and Danijel Skočaj. Transfusion—a transparency-based diffusion model for anomaly detection. In *European conference on computer vision*, pages 91–108. Springer, 2024.
- [19] Haifan Gong, Guanqi Chen, Ranran Wang, Xiang Xie, Mingzhi Mao, Yizhou Yu, Fei Chen, and Guanbin Li. Multi-task learning for thyroid nodule segmentation with thyroid region prior. In *2021 IEEE 18th international symposium on biomedical imaging (ISBI)*, pages 257–261. IEEE, 2021.
- [20] Zhihao Gu, Liang Liu, Xu Chen, Ran Yi, Jiangning Zhang, Yabiao Wang, Chengjie Wang, Annan Shu, Guannan Jiang, and Lizhuang Ma. Remembering normality: Memory-guided knowledge distillation for unsupervised anomaly detection. In *Proceedings of the IEEE/CVF International Conference on Computer Vision*, pages 16401–16409, 2023.
- [21] Denis Gudovskiy, Shun Ishizaka, and Kazuki Kozuka. Cflow-ad: Real-time unsupervised anomaly detection with localization via conditional normalizing flows. In *Proceedings of the*

- IEEE/CVF winter conference on applications of computer vision*, pages 98–107, 2022.
- [22] David Gutman, Noel C. F. Codella, Emre Celebi, Brian Helba, Michael Marchetti, Nabin Mishra, and Allan Halpern. Skin lesion analysis toward melanoma detection: A challenge at the international symposium on biomedical imaging (isbi) 2016, hosted by the international skin imaging collaboration (isic), 2016.
- [23] Ahmed Hamada. Br35h: Brain tumor detection 2020, 2020.
- [24] Steven Hicks, Debesh Jha, Vajira Thambawita, Pål Halvorsen, Hugo Hammer, and Michael Riegler. *The EndoTect 2020 Challenge: Evaluation and Comparison of Classification, Segmentation and Inference Time for Endoscopy*, pages 263–274. 2021.
- [25] Teng Hu, Jiangning Zhang, Ran Yi, Yuzhen Du, Xu Chen, Liang Liu, Yabiao Wang, and Chengjie Wang. Anomalydiffusion: Few-shot anomaly image generation with diffusion model. In *Proceedings of the AAAI conference on artificial intelligence*, pages 8526–8534, 2024.
- [26] Jongheon Jeong, Yang Zou, Taewan Kim, Dongqing Zhang, Avinash Ravichandran, and Onkar Dabeer. Winclip: Zero/few-shot anomaly classification and segmentation. In *Proceedings of the IEEE/CVF Conference on Computer Vision and Pattern Recognition*, pages 19606–19616, 2023.
- [27] Stepan Jezek, Martin Jonak, Radim Burget, Pavel Dvorak, and Milos Skotak. Deep learning-based defect detection of metal parts: evaluating current methods in complex conditions. In *2021 13th International congress on ultra modern telecommunications and control systems and workshops (ICUMT)*, pages 66–71. IEEE, 2021.
- [28] Pranita Balaji Kanade and PP Gumaste. Brain tumor detection using mri images. *Brain*, 3(2):146–150, 2015.
- [29] Alexander Kirillov, Eric Mintun, Nikhila Ravi, Hanzi Mao, Chloe Rolland, Laura Gustafson, Tete Xiao, Spencer Whitehead, Alexander C Berg, Wan-Yen Lo, et al. Segment anything. In *Proceedings of the IEEE/CVF international conference on computer vision*, pages 4015–4026, 2023.
- [30] Felipe Campos Kitamura. Head ct - hemorrhage, 2018.
- [31] Mengcheng Lan, Chaofeng Chen, Yiping Ke, Xinjiang Wang, Litong Feng, and Wayne Zhang. Clearclip: Decomposing clip representations for dense vision-language inference. In *European Conference on Computer Vision*, pages 143–160. Springer, 2024.
- [32] Mengcheng Lan, Chaofeng Chen, Yiping Ke, Xinjiang Wang, Litong Feng, and Wayne Zhang. Proxyclip: Proxy attention improves clip for open-vocabulary segmentation. In *European Conference on Computer Vision*, pages 70–88. Springer, 2024.
- [33] Junnan Li, Dongxu Li, Caiming Xiong, and Steven Hoi. BLIP: Bootstrapping language-image pre-training for unified vision-language understanding and generation. In *Proceedings of the 39th International Conference on Machine Learning*, pages 12888–12900. PMLR, 2022.
- [34] Shengze Li, Jianjian Cao, Peng Ye, Yuhan Ding, Chongjun Tu, and Tao Chen. Clipsam: Clip and sam collaboration for zero-shot anomaly segmentation. *Neurocomputing*, 618: 129122, 2025.
- [35] Xiaofan Li, Zhizhong Zhang, Xin Tan, Chengwei Chen, Yanyun Qu, Yuan Xie, and Lizhuang Ma. Promptad: Learning prompts with only normal samples for few-shot anomaly detection. In *Proceedings of the IEEE/CVF Conference on Computer Vision and Pattern Recognition*, pages 16838–16848, 2024.
- [36] Yi Li, Hualiang Wang, Yiqun Duan, and Xiaomeng Li. Clip surgery for better explainability with enhancement in open-vocabulary tasks. *arXiv e-prints*, pages arXiv–2304, 2023.
- [37] Tsung-Yi Lin, Priya Goyal, Ross Girshick, Kaiming He, and Piotr Dollár. Focal loss for dense object detection. In *Proceedings of the IEEE international conference on computer vision*, pages 2980–2988, 2017.
- [38] Jiaqi Liu, Guoyang Xie, Jinbao Wang, Shangnian Li, Chengjie Wang, Feng Zheng, and Yaochu Jin. Deep industrial image anomaly detection: A survey. *Machine Intelligence Research*, 21(1):104–135, 2024.
- [39] Zhikang Liu, Yiming Zhou, Yuansheng Xu, and Zilei Wang. Simplenet: A simple network for image anomaly detection and localization. In *Proceedings of the IEEE/CVF conference on computer vision and pattern recognition*, pages 20402–20411, 2023.
- [40] Hossein Mirzaei, Mohammadreza Salehi, Sajjad Shahabi, Efstratios Gavves, Cees G. M. Snoek, Mohammad Sabokrou, and Mohammad Hossein Rohban. Fake it until you make it : Towards accurate near-distribution novelty detection. In *The Eleventh International Conference on Learning Representations*, 2023.
- [41] Pankaj Mishra, Riccardo Verk, Daniele Fornasier, Claudio Piciarelli, and Gian Luca Foresti. Vt-adl: A vision transformer network for image anomaly detection and localization. In *2021 IEEE 30th International Symposium on Industrial Electronics (ISIE)*, pages 01–06. IEEE, 2021.
- [42] Maxime Oquab, Timothée Darcet, Théo Moutakanni, Huy Vo, Marc Szafraniec, Vasil Khalidov, Pierre Fernandez, Daniel Haziza, Francisco Massa, Alaaeldin El-Nouby, et al. Dinov2: Learning robust visual features without supervision. *arXiv preprint arXiv:2304.07193*, 2023.
- [43] Maxime Oquab, Timothée Darcet, Théo Moutakanni, Huy Vo, Marc Szafraniec, Vasil Khalidov, Pierre Fernandez, Daniel Haziza, Francisco Massa, Alaaeldin El-Nouby, et al. Dinov2: Learning robust visual features without supervision. *arXiv preprint arXiv:2304.07193*, 2023.
- [44] Guansong Pang, Chunhua Shen, and Anton Van Den Hengel. Deep anomaly detection with deviation networks. In *Proceedings of the 25th ACM SIGKDD international conference on knowledge discovery & data mining*, pages 353–362, 2019.
- [45] Zhen Qu, Xian Tao, Mukesh Prasad, Fei Shen, Zhengtao Zhang, Xinyi Gong, and Guiguang Ding. Vcp-clip: A visual context prompting model for zero-shot anomaly segmentation. In *European Conference on Computer Vision*, pages 301–317. Springer, 2024.
- [46] Alec Radford, Jong Wook Kim, Chris Hallacy, Aditya Ramesh, Gabriel Goh, Sandhini Agarwal, Girish Sastry, Amanda Askell, Pamela Mishkin, Jack Clark, et al. Learning transferable visual models from natural language supervision. In *International conference on machine learning*, pages 8748–8763. PmlR, 2021.

- [47] Karsten Roth, Latha Pemula, Joaquin Zepeda, Bernhard Schölkopf, Thomas Brox, and Peter Gehler. Towards total recall in industrial anomaly detection. In *Proceedings of the IEEE/CVF conference on computer vision and pattern recognition*, pages 14318–14328, 2022.
- [48] Shuvendu Roy and Ali Etemad. Consistency-guided prompt learning for vision-language models. *arXiv preprint arXiv:2306.01195*, 2023.
- [49] Lukas Ruff, Robert A Vandermeulen, Nico Görnitz, Alexander Binder, Emmanuel Müller, Klaus-Robert Müller, and Marius Kloft. Deep semi-supervised anomaly detection. *arXiv preprint arXiv:1906.02694*, 2019.
- [50] Lukas Ruff, Jacob R Kauffmann, Robert A Vandermeulen, Grégoire Montavon, Wojciech Samek, Marius Kloft, Thomas G Dietterich, and Klaus-Robert Müller. A unifying review of deep and shallow anomaly detection. *Proceedings of the IEEE*, 109(5):756–795, 2021.
- [51] Mohammadreza Salehi, Hossein Mirzaei, Dan Hendrycks, Yixuan Li, Mohammad Hossein Rohban, and Mohammad Sabokrou. A unified survey on anomaly, novelty, open-set, and out-of-distribution detection: Solutions and future challenges. *arXiv preprint arXiv:2110.14051*, 2021.
- [52] Mohammadreza Salehi, Hossein Mirzaei, Dan Hendrycks, Yixuan Li, Mohammad Hossein Rohban, and Mohammad Sabokrou. A unified survey on anomaly, novelty, open-set, and out-of-distribution detection: Solutions and future challenges. *arXiv preprint arXiv:2110.14051*, 2021.
- [53] Mohammadreza Salehi, Niousha Sadjadi, Soroosh Baselizadeh, Mohammad H Rohban, and Hamid R Rabiee. Multiresolution knowledge distillation for anomaly detection. In *Proceedings of the IEEE/CVF conference on computer vision and pattern recognition*, pages 14902–14912, 2021.
- [54] Luc PJ Sträter, Mohammadreza Salehi, Efstathios Gavves, Cees GM Snoek, and Yuki M Asano. Generalad: Anomaly detection across domains by attending to distorted features. In *European Conference on Computer Vision*, pages 448–465. Springer, 2024.
- [55] Carole H Sudre, Wenqi Li, Tom Vercauteren, Sebastien Ourselin, and M Jorge Cardoso. Generalised dice overlap as a deep learning loss function for highly unbalanced segmentations. In *Deep Learning in Medical Image Analysis and Multimodal Learning for Clinical Decision Support: Third International Workshop, DLMIA 2017, and 7th International Workshop, ML-CDS 2017, Held in Conjunction with MICCAI 2017, Québec City, QC, Canada, September 14, Proceedings 3*, pages 240–248. Springer, 2017.
- [56] Domen Tabernik, Samo Šela, Jure Skvarč, and Danijel Skočaj. Segmentation-based deep-learning approach for surface-defect detection. *Journal of Intelligent Manufacturing*, 31(3):759–776, 2020.
- [57] Nima Tajbakhsh, Suryakanth R Gurudu, and Jianming Liang. Automated polyp detection in colonoscopy videos using shape and context information. *IEEE transactions on medical imaging*, 35(2):630–644, 2015.
- [58] Matthias Wieler and Tobias Hahn. Weakly supervised learning for industrial optical inspection. In *DAGM symposium in*, 2007.
- [59] Hang Yao, Ming Liu, Zhicun Yin, Zifei Yan, Xiaopeng Hong, and Wangmeng Zuo. Glad: towards better reconstruction with global and local adaptive diffusion models for unsupervised anomaly detection. In *European Conference on Computer Vision*, pages 1–17. Springer, 2024.
- [60] Xincheng Yao, Ruoqi Li, Jing Zhang, Jun Sun, and Chongyang Zhang. Explicit boundary guided semi-push-pull contrastive learning for supervised anomaly detection. In *Proceedings of the IEEE/CVF Conference on Computer Vision and Pattern Recognition*, pages 24490–24499, 2023.
- [61] Jiawei Yu, Ye Zheng, Xiang Wang, Wei Li, Yushuang Wu, Rui Zhao, and Liwei Wu. Fastflow: Unsupervised anomaly detection and localization via 2d normalizing flows. *arXiv preprint arXiv:2111.07677*, 2021.
- [62] Xiaohua Zhai, Xiao Wang, Basil Mustafa, Andreas Steiner, Daniel Keysers, Alexander Kolesnikov, and Lucas Beyer. Lit: Zero-shot transfer with locked-image text tuning. In *Proceedings of the IEEE/CVF conference on computer vision and pattern recognition*, pages 18123–18133, 2022.
- [63] Hui Zhang, Zheng Wang, Zuxuan Wu, and Yu-Gang Jiang. Diffusionad: Norm-guided one-step denoising diffusion for anomaly detection. *arXiv preprint arXiv:2303.08730*, 2023.
- [64] Hui Zhang, Zuxuan Wu, Zheng Wang, Zhineng Chen, and Yu-Gang Jiang. Prototypical residual networks for anomaly detection and localization. In *Proceedings of the IEEE/CVF Conference on Computer Vision and Pattern Recognition*, pages 16281–16291, 2023.
- [65] Kaiyang Zhou, Jingkang Yang, Chen Change Loy, and Ziwei Liu. Learning to prompt for vision-language models. *International Journal of Computer Vision*, 130(9):2337–2348, 2022.
- [66] Qihang Zhou, Guansong Pang, Yu Tian, Shibo He, and Jiming Chen. Anomalyclip: Object-agnostic prompt learning for zero-shot anomaly detection. In *ICLR*, 2024.
- [67] Jiawen Zhu and Guansong Pang. Toward generalist anomaly detection via in-context residual learning with few-shot sample prompts. In *Proceedings of the IEEE/CVF conference on computer vision and pattern recognition*, pages 17826–17836, 2024.
- [68] Yang Zou, Jongheon Jeong, Latha Pemula, Dongqing Zhang, and Onkar Dabeer. Spot-the-difference self-supervised pre-training for anomaly detection and segmentation. In *European Conference on Computer Vision*, pages 392–408. Springer, 2022.

Appendix

A. Implementation Details

In this study, we use the publicly available pre-trained CLIP (ViT-L/14@336px)¹ as the default backbone and pre-trained DINOv2-B14² for further spatial alignment. Each input prompt is assigned 12 learnable token embeddings, while 4 learnable deep token embeddings per layer are inserted into the first 9 layers of the text encoder. Input images to the vision tower are resized to 518×518 and undergo the same normalization for both training and inference. All experiments are conducted using PyTorch 1.13.1 on a single NVIDIA Titan XP 12GB GPU.

To evaluate zero-shot anomaly detection performance, we fine-tune *Crane* on the test set of MVTec-AD and assess its generalization across other datasets. For evaluation on MVTec-AD, the model is trained on the test data of VisA. MVTec-AD and VisA contain distinct object categories with no overlap with the samples in other datasets, and the benchmark datasets used in this study span diverse domains, ensuring minimal category overlap across datasets.

B. State-of-the-Art Methods

We compare our proposed model with five state-of-the-art methods from the literature. An intuition of their approach and reproduction details is as follows:

- **WinCLIP [26]**: A zero-/few-shot anomaly classification and segmentation model using a pre-trained CLIP model. It processes multi-scale input image segments and compares them with text embeddings from predefined prompts describing normal and anomalous states. The model aggregates multi-scale spatial features aligned with language for final anomaly segmentation. Metrics such as AUROC, PRO, and F1-Max on MVTec-AD and VisA are from the original publication, while other metrics and datasets are reproduced using the unofficial implementation³.
- **AnoVL [13]**: Adapts vision-language models for zero-shot anomaly detection by optimizing model parameters through test-time adaptation. It uses v-v attention [36] to address spatial misalignment of textual and patch embeddings. AUROC, PRO, and F1-Max values on MVTec-AD and VisA are from the original paper; other metrics and datasets are derived from the official code implementation.
- **VAND [10]**: Utilizes a vision encoder fine-tuning strategy with linear projections atop features from an auxiliary training set. Its textual prompting approach is similar to WinCLIP and AnoVL. Metrics for MVTec-AD and VisA are from the original publication. For datasets without official measurements, results are reproduced using default parameters from their paper.

¹https://github.com/mlfoundations/open_clip

²<https://github.com/facebookresearch/dinov2>

³<https://github.com/caoyunkang/WinClip>

- **AnomalyCLIP [66]**: Introduces object-agnostic learnable prompts for zero-shot anomaly detection. By using a general [object] token in text prompts, it emphasizes anomalous regions across domains, enhancing generalization without category-specific training. The original paper provides metrics for all datasets except F1-Max, which are reproduced using the official codebase and default parameters.
- **AdaCLIP [7]**: Adapts CLIP for zero-shot anomaly detection by incorporating learnable deep tokens into vision and text encoders. It uses static and dynamic prompts; static prompts are shared across images for preliminary adaptation, while dynamic prompts are image-specific. The original paper provides metrics for all datasets except AUPRO and Image-AP, which are reproduced using the official codebase and default parameters.

C. Datasets

For a comprehensive evaluation of the zero-shot generalization capabilities of the proposed model, we conduct experiments across test set of 14 diverse datasets, encompassing two domains (industrial and medical) and three modalities (photography, radiology, and endoscopy). Table 4 provides a detailed listing of the statistical details, application, modality, and anomaly pattern types. As shown, some datasets are solely applicable for anomaly localization or detection because they either contain only abnormal images with segmentation masks (e.g., CVC-ColonDB) or include both normal and abnormal samples but lack pixel-level masks.

D. Ablation Studies on Medical Training

Building on the remarkable performance of the model when applied to medical datasets—despite being trained solely on an industrial dataset with significant texture differences—we examine the model’s behavior when medical samples are included in training, while the test domain remains unexposed. Following the approach in [66], we combine the test split of the classification EndoTect [24] with CVC-ColonDB [57] and evaluate on other medical datasets. For evaluation on CVC-ColonDB, we train the model on CVC-ClinicDB [4] and test it on the EndoTect test dataset. Although both CVC-ColonDB and CVC-ClinicDB consist of colonoscopy images, they were captured using different endoscopic equipment, resulting in variations in image quality and texture.

Table 5 shows the performance of the selected models under the aforementioned training scheme. With respect to the default evaluation in Main Table 2, *Crane*’s performance in pixel-level anomaly detection improved by 12.1% in F1-max and 5.6% in AUROC. At the image level, it demonstrates a 2.3% increase in F1-max and a 1.5% increase in AUROC. Moreover, in the current table, *Crane* exceeds the second-best model by 5.4 points in AUROC and 5.2 points in F1-max for pixel-level performance. At the image level, it outper-

Table 4. **Numerical details of the utilized datasets.** $|C|$ indicates the number of object categories in each dataset. The "Labels" column specifies whether the dataset contains image-level and/or pixel-level annotations.

Category	Dataset	Type	Modalities	$ C $	# Normal & Anomalous	Detection	Task	
							detection	localization
Industrial	MVTec AD	Obj & texture	Photography	15	(467, 1258)	Industrial defect	✓	✓
	VisA	Obj	Photography	12	(962, 1200)	Industrial defect	✓	✓
	MPDD		Photography	6	(176, 282)	Industrial defect	✓	✓
	BTAD		Photography	3	(451, 290)	Industrial defect	✓	✓
	SDD		Photography	1	(181, 74)	Industrial defect	✓	✓
	DAGM	Texture	Photography	10	(6996, 1054)	Industrial defect	✓	✓
DTD-Synthetic	Photography		12	(357, 947)	Industrial defect	✓	✓	
Medical	ISIC	Skin	Photography	1	(0, 379)	Skin cancer	✗	✓
	CVC-ClinicDB	Colon	Endoscopy	1	(0, 612)	Colon polyp	✗	✓
	CVC-ColonDB		Endoscopy	1	(0, 380)	Colon polyp	✗	✓
	Endo		Endoscopy	1	(0, 200)	Colon polyp	✓	✗
	TN3K	Thyroid	Radiology (Ultrasound)	1	(0, 614)	Thyroid nodule	✗	✓
	HeadCT	Brain	Radiology (CT)	1	(100, 100)	Brain tumor	✓	✗
	BrainMRI		Radiology (MRI)	1	(98, 155)	Brain tumor	✓	✗
	Br35H		Radiology (MRI)	1	(1500, 1500)	Brain tumor	✓	✗

Table 5. **Comparisons of ZSAD methods in the medical domain, Supervised models are trained on medical datasets.** The best performance is **bold**, and the second-best is underlined.

Metric	Dataset	WinCLIP [†] [26]	AnoVL [†] [13]	VAND[10]	AnomalyCLIP[66]	AdaCLIP[7]	Ours
Image-level (AUROC, AP, F1-max)	HeadCT	(81.8, 80.2, 79.8)	(82.3, 81.2, 79.1)	(89.2, 89.5, 82.1)	<u>(93.5, 95.1, 91.7)</u>	(81.5, 85.9, 75.3)	(96.8, 97.5, 92.0)
	BrainMRI	(86.6, 91.5, 86.3)	(84.3, 89.2, 84.8)	(89.6, 91.0, 88.5)	<u>(95.5, 97.2, 93.5)</u>	(61.5, 73.5, 76.6)	(97.8, 98.7, 95.3)
	Br35H	(80.5, 82.2, 74.4)	(80.0, 80.7, 75.2)	(91.4, 91.9, 84.2)	(97.9, 98.0, 92.5)	(52.4, 58.3, 67.5)	<u>(97.3, 98.1, 93.7)</u>
	Average	(83.0, 84.6, 80.2)	(82.2, 83.7, 79.7)	(90.1, 90.8, 84.9)	<u>(95.6, 96.8, 92.6)</u>	(65.1, 72.6, 73.1)	(97.3, 98.1, 93.7)
Pixel-level (AUROC, AUPRO, F1-max)	ISIC	(83.3, 55.1, 48.5)	(92.6, 82.2, 76.6)	(83.1, 70.5, 63.7)	(83.0, 63.8, 66.1)	(72.8, 3.23, 55.0)	<u>(91.5, 84.1, 77.6)</u>
	ColonDB	(70.3, 32.5, 19.6)	(76.2, 44.1, 26.8)	<u>(88.7, 82.5, 58.8)</u>	(87.5, 78.5, 52.1)	(85.5, 24.1, 56.3)	(94.2, 85.3, 59.3)
	ClinicDB	(51.2, 13.8, 24.4)	(79.7, 51.4, 36.3)	(93.5, 86.6, 71.9)	<u>(92.4, 82.9, 60.0)</u>	(92.3, 54.1, 69.6)	(91.3, 84.6, 69.1)
	TN3K	(70.7, 39.8, 30.0)	(70.2, 34.4, 32.3)	(76.9, 37.2, 40.5)	<u>(79.2, 47.0, 47.6)</u>	(52.4, 0.45, 23.0)	(87.2, 54.8, 49.6)
	Average	(68.9, 35.3, 30.6)	(79.7, 53.0, 43.0)	<u>(85.6, 69.2, 58.7)</u>	(85.5, 68.1, 56.4)	(75.8, 20.5, 51.0)	(91.0, 77.2, 63.9)

forms the second-best model by 1.7 points in AUROC and 1.3 points in F1-max.

D. Category-level Results

In this section, quantitative and qualitative sub-datasets reproduction results across different categories of evaluation datasets are reported. The reproduction is conducted according to the details stated in the [Appendix B](#).

D.1 Category-level Quantative Results

Table 6. **Category-level anomaly localization performance for the dataset BTAD.** each triplet reports (AUROC, AUPRO, F1-max).

Product	AnVoL	VAND	AnomalyCLIP	AdaCLIP	Crane w/o D-Attn	Crane
01	(93.8, 56.0, 46.2)	(89.9, 72.3, 53.3)	(93.7, 73.0, 52.9)	(88.8, 1.60, 54.1)	(96.2, 77.3, 60.8)	(97.0, 84.0, 65.5)
02	(57.8, 15.8, 17.1)	(86.3, 50.3, 56.7)	(94.4, 66.0, 60.0)	(95.9, 12.0, 64.0)	(95.7, 72.8, 64.0)	(95.0, 81.1, 66.7)
03	(74.0, 50.9, 6.90)	(91.8, 83.6, 12.0)	(94.6, 87.1, 36.4)	(96.3, 47.0, 38.4)	(97.9, 93.6, 45.9)	(97.9, 95.5, 51.3)
Mean	(75.2, 40.9, 23.4)	(89.3, 68.7, 40.6)	(94.2, 75.4, 49.7)	(92.9, 22.8, 48.1)	(96.6, 81.3, 56.9)	(96.7, 86.9, 61.2)

Table 7. **Category-level anomaly classification performance for the dataset BTAD.** each triplet reports (AUROC, AP, F1-max).

Product	AnVoL	VAND	AnomalyCLIP	AdaCLIP	Crane w/o D-Attn	Crane
01	(94.8, 97.9, 92.8)	(82.0, 92.3, 84.3)	(90.9, 96.6, 89.4)	(93.2, 95.6, 91.8)	(98.3, 99.3, 95.7)	(98.2, 99.3, 96.8)
02	(65.4, 93.8, 93.0)	(82.0, 96.8, 93.5)	(84.1, 97.4, 93.3)	(80.3, 94.8, 87.2)	(86.6, 97.9, 93.7)	(92.2, 98.8, 94.7)
03	(80.7, 27.6, 33.2)	(57.5, 19.8, 26.4)	(89.8, 70.7, 68.6)	(97.6, 93.6, 85.6)	(98.3, 90.5, 85.7)	(98.5, 92.6, 87.2)
Mean	(80.3, 72.8, 73.0)	(73.8, 69.6, 68.1)	(88.2, 87.3, 83.8)	(88.7, 93.8, 88.2)	(94.4, 95.9, 91.7)	(96.3, 96.9, 92.9)

Table 8. **Category-level anomaly localization performance for the dataset DAGM.** each triplet reports (AUROC, AUPRO, F1-max).

Product	AnVoL	VAND	AnomalyCLIP	AdaCLIP	Crane w/o D-Attn	Crane
Class01	(58.0, 18.1, 2.0)	(70.5, 52.0, 32.5)	(88.0, 76.7, 50.2)	(83.5, 58.8, 44.8)	(88.3, 72.7, 48.5)	(86.6, 75.7, 40.2)
Class02	(90.0, 75.5, 16.4)	(88.1, 83.5, 51.1)	(99.5, 99.1, 64)	(96.2, 66.5, 66.6)	(99.6, 98.2, 73.1)	(98.7, 98.8, 72.5)
Class03	(86.8, 62.2, 7.2)	(78.5, 61.5, 36.7)	(95.9, 93.8, 69.7)	(96.2, 44.3, 72.7)	(95.8, 89.9, 73.2)	(95.6, 93.6, 70.5)
Class04	(79.4, 54.7, 8.1)	(75.5, 44.1, 5.3)	(89.1, 75.3, 35.6)	(86.7, 17.1, 9.6)	(92.5, 80.8, 35.6)	(93.9, 86.4, 33.6)
Class05	(81.8, 56.5, 13.5)	(82.3, 64.0, 54.9)	(99.1, 96.9, 74.2)	(97.5, 52.0, 76.7)	(99.1, 94.6, 79.5)	(99.3, 98.1, 80.5)
Class06	(93.1, 81.2, 47.6)	(91.9, 81.7, 74.5)	(99.1, 96.0, 76.4)	(99.1, 61.5, 82.7)	(99.3, 93.2, 78.8)	(99.8, 99.1, 82.8)
Class07	(63.3, 26.9, 3.5)	(83.6, 69.6, 54.2)	(90.3, 86.5, 70)	(93.3, 57.4, 72.1)	(90.5, 87.8, 72.8)	(89.9, 88.7, 70.9)
Class08	(58.6, 23.0, 0.3)	(80.2, 64.1, 12.1)	(98.3, 96.3, 55.7)	(93.5, 40.1, 64.4)	(99.0, 98.4, 68.4)	(99.6, 99.6, 68.7)
Class09	(89.2, 70.1, 3.9)	(90.6, 78.6, 26.9)	(98.3, 92.7, 33.5)	(94.9, 60.8, 44.0)	(99.9, 99.2, 76.0)	(99.9, 99.6, 75.2)
Class10	(97.0, 91.6, 25.7)	(83.0, 61.1, 25.5)	(98.5, 97.1, 60.1)	(96.1, 47.5, 61.2)	(98.8, 97.1, 66.5)	(99.2, 98.9, 73.4)
Mean	(79.7, 56.0, 12.8)	(82.4, 66.0, 37.4)	(95.6, 91.0, 58.9)	(93.7, 50.6, 59.5)	(96.3, 91.2, 67.2)	(96.2, 93.8, 66.8)

Table 9. **Category-level anomaly classification performance for the dataset DAGM.** each triplet reports (AUROC, AP, F1-max).

Product	AnVoL	VAND	AnomalyCLIP	AdaCLIP	Crane w/o D-Attn	Crane
Class01	(58.3, 22.8, 30.8)	(79.9, 37.0, 38.2)	(85.8, 49.8, 52.6)	(88.3, 44.2, 51.5)	(92.8, 78.8, 73.2)	(89.9, 66.8, 65.2)
Class02	(99.4, 98.1, 95.1)	(95.0, 87.0, 81.3)	(100, 100, 100)	(99.5, 98.5, 95.9)	(100, 100, 100)	(100, 100, 100)
Class03	(99.6, 97.9, 93.0)	(99.4, 96.6, 91.4)	(99.9, 99.5, 97)	(100, 100, 100)	(100, 100, 100)	(100, 100, 100)
Class04	(89.9, 74.5, 54.3)	(85.2, 66.4, 48.6)	(97.6, 94.1, 85.7)	(95.8, 89.2, 79.4)	(99.4, 98.5, 96.4)	(99.0, 98.1, 93.2)
Class05	(95.7, 87.4, 72.8)	(94.6, 82.2, 65.9)	(99.2, 98.1, 100)	(98.9, 94.3, 90.2)	(100, 100, 100)	(99.9, 99.6, 98.2)
Class06	(99.1, 95.8, 87.3)	(98.5, 92.4, 81.6)	(99.8, 99.4, 100)	(99.9, 98.7, 96.1)	(100, 100, 100)	(100, 99.9, 99.1)
Class07	(78.8, 54.6, 40.5)	(86.1, 70.9, 58.3)	(95.3, 90.5, 94.8)	(94.7, 82.8, 73.6)	(100, 100, 99.7)	(98.3, 96.0, 90.7)
Class08	(81.5, 60.3, 44.9)	(90.3, 78.7, 67.2)	(97.7, 95.2, 87.1)	(96.5, 89.1, 83.1)	(99.8, 99.0, 96.3)	(99.5, 98.8, 96.7)
Class09	(92.4, 83.2, 68.1)	(94.8, 88.0, 75.5)	(99.0, 98.3, 86.1)	(98.7, 96.8, 92.5)	(99.7, 98.3, 93.4)	(99.9, 99.7, 98.4)
Class10	(96.8, 90.5, 80.2)	(92.0, 82.1, 70.7)	(98.9, 97.5, 97.6)	(98.5, 95.6, 89.8)	(100, 99.8, 99.0)	(99.8, 99.3, 98.0)
Mean	(89.7, 76.1, 74.7)	(94.4, 83.9, 79.9)	(97.7, 92.4, 90.1)	(96.9, 88.5, 87.7)	(99.2, 97.4, 95.8)	(98.9, 96.1, 94.7)

Table 10. **Category-level anomaly localization performance for the dataset DTD-Syn.** each triplet reports (AUROC, AUPRO, F1-max).

Product	AnVoL	VAND	AnomalyCLIP	AdaCLIP	Crane w/o D-Attn	Crane
Woven_001	(93.0, 75.6, 33.8)	(99.2, 82.6, 77.9)	(99.7, 98.9, 67.2)	(99.9, 87.1, 78.0)	(99.8, 99.1, 72.7)	(99.9, 99.4, 75.0)
Woven_127	(89.4, 74.9, 19.1)	(90.8, 55.6, 60.2)	(93.7, 89.5, 51.9)	(96.0, 65.3, 64.2)	(95.6, 94.7, 63.6)	(95.3, 93.7, 65.9)
Woven_104	(96.1, 86.5, 41.5)	(94.3, 69.5, 68.9)	(96.1, 92.5, 63.1)	(98.6, 79.4, 73.1)	(98.4, 96.7, 68.7)	(98.6, 96.8, 70.9)
Stratified_154	(99.2, 94.6, 61.1)	(96.8, 77.6, 78.6)	(99.5, 96.2, 67.4)	(97.5, 76.5, 72.4)	(99.5, 99.0, 72.3)	(99.3, 98.3, 72.9)
Blotchy_099	(94.4, 84.1, 37.3)	(99.0, 71.0, 68.5)	(99.5, 96.2, 67.5)	(99.7, 87.3, 79.2)	(99.6, 96.5, 73.2)	(99.7, 97.2, 76.0)
Woven_068	(97.2, 89.1, 33.1)	(95.2, 63.4, 62.9)	(98.7, 92.8, 47.8)	(98.4, 65.1, 60.7)	(98.7, 95.7, 51.6)	(99.1, 96.9, 61.4)
Woven_125	(90.4, 80.8, 33.8)	(98.8, 84.6, 83.5)	(99.4, 95.6, 64.1)	(99.8, 90.6, 82.5)	(99.6, 97.9, 70.5)	(99.7, 99.1, 75.5)
Marbled_078	(97.7, 92, 43.6)	(98.1, 77.4, 73.3)	(99.1, 97.1, 62)	(99.6, 85.2, 77.1)	(99.4, 97.7, 68.3)	(99.4, 97.6, 71.3)
Perforated_037	(98.8, 95.9, 46.3)	(89.0, 61.0, 68.1)	(94.6, 85.1, 63.1)	(96.4, 70.6, 69.2)	(96.6, 94.1, 70.0)	(97.9, 96.5, 71.7)
Mesh_114	(83.4, 57.7, 26.4)	(89.0, 60.6, 66.4)	(95.2, 77.0, 56.5)	(97.7, 73.7, 70.0)	(95.2, 83.3, 64.8)	(97.0, 88.7, 68.1)
Fibrous_183	(93.8, 80.2, 35.6)	(97.5, 56.1, 55.7)	(99.4, 98.2, 69.2)	(99.0, 82.1, 75.0)	(99.7, 99.2, 78.6)	(99.7, 99.1, 77.1)
Matted_069	(86.1, 61.6, 17.5)	(95.2, 44.1, 45.1)	(99.6, 84.8, 66.7)	(98.5, 56.4, 55.5)	(99.7, 88.4, 74.5)	(99.7, 89.2, 75.9)
Mean	(93.3, 81.1, 35.8)	(95.2, 66.9, 67.4)	(97.9, 92.0, 62.2)	(98.4, 76.6, 71.4)	(98.5, 95.2, 69.1)	(98.8, 96.0, 71.8)

Table 11. **Category-level anomaly classification performance for the dataset DTD-Syn.** each triplet reports (AUROC, AP, F1-max).

Product	AnVoL	VAND	AnomalyCLIP	AdaCLIP	Crane w/o D-Attn	Crane
Woven_001	(96.7, 94.0, 98.7)	(96.1, 95.5, 98.6)	(100, 100, 100)	(100, 100, 100)	(99.4, 99.9, 98.7)	(98.4, 99.6, 97.5)
Woven_127	(80.8, 77.9, 83.8)	(74.4, 70.2, 77.8)	(80.7, 83.5, 76.2)	(99.8, 99.9, 98.8)	(100, 100, 100)	(98.6, 99.7, 98.1)
Woven_104	(94.8, 93.9, 98.7)	(76.2, 89.9, 93.7)	(98.1, 99.6, 97.5)	(97.9, 99.4, 98.2)	(98.6, 99.7, 98.7)	(100, 100, 99.3)
Stratified_154	(99.8, 98.8, 99.9)	(97.4, 96.3, 99.4)	(97.6, 99.4, 95.8)	(91.7, 97.7, 95.1)	(99.7, 99.9, 98.8)	(99.8, 100, 99.4)
Blotchy_099	(99.3, 98.7, 99.8)	(92.6, 92.0, 98.2)	(98.9, 99.7, 98.8)	(89.6, 95.4, 90.5)	(92.6, 94.3, 87.4)	(90.5, 92.6, 83.3)
Woven_068	(86.2, 81.7, 92.6)	(84.5, 80.0, 91.6)	(96.9, 98.4, 94.9)	(92.6, 98.2, 93.1)	(99.0, 99.8, 98.8)	(100, 100, 100)
Woven_125	(99.7, 99.4, 99.9)	(94.3, 93.9, 98.5)	(99.8, 100, 99.4)	(99.4, 99.9, 98.1)	(100, 100, 100)	(98.9, 99.8, 98.8)
Marbled_078	(98.7, 98.1, 99.7)	(98.8, 98.1, 99.7)	(98.7, 99.7, 97.5)	(99.1, 99.6, 97.8)	(93.7, 98.5, 93.3)	(95.2, 98.9, 94.5)
Perforated_037	(99.9, 99.4, 100)	(75.1, 88.9, 92.9)	(90.6, 97.5, 92.5)	(89.5, 94.0, 84.7)	(87.6, 95.1, 86.6)	(88.3, 95.2, 85.9)
Mesh_114	(88.2, 86.1, 95.4)	(72.7, 81.7, 87.7)	(85.8, 94.5, 84.4)	(99.3, 99.8, 99.4)	(95.1, 97.3, 91.0)	(94.8, 97.2, 90.5)
Fibrous_183	(98.1, 97.5, 99.6)	(89.4, 92.8, 97.2)	(97.2, 99.3, 95.7)	(100, 100, 100)	(99.1, 99.8, 97.5)	(97.3, 99.4, 96.2)
Matted_069	(96.6, 94.6, 99.2)	(74.7, 88.8, 92.5)	(82.6, 95.2, 91.2)	(85.1, 83.5, 81.8)	(91.1, 97.8, 92.2)	(87.8, 96.8, 91.8)
Mean	(94.9, 93.3, 97.3)	(85.5, 89.0, 94.0)	(93.9, 97.2, 93.6)	(95.3, 97.3, 94.8)	(96.3, 98.5, 95.3)	(95.8, 98.3, 94.6)

Table 12. **Category-level anomaly localization performance for the dataset MPDD.** each triplet reports (AUROC, AUPRO, F1-max).

Product	AnVoL	VAND	AnomalyCLIP	AdaCLIP	Crane w/o D-Attn	Crane
bracket_black	(24.6, 1.6, 0.2)	(96.3, 90.6, 15.8)	(95.7, 85.2, 27.2)	(96.5, 82.6, 14.4)	(96.1, 86.1, 28.6)	(97.2, 90.4, 30.4)
bracket_brown	(27.4, 3.4, 1.0)	(87.4, 72.6, 8.7)	(94.4, 77.8, 13.1)	(93.3, 28.7, 18.8)	(99.8, 96.2, 35.1)	(99.8, 97.7, 31.4)
bracket_white	(45.2, 1.7, 0.1)	(99.2, 93.7, 8.9)	(99.8, 98.8, 22.9)	(98.1, 63.9, 6.9)	(97.7, 92.2, 25.2)	(98.0, 95.5, 36.6)
connector	(90.0, 68.2, 4.7)	(90.6, 74.5, 22.5)	(97.2, 89.9, 27.0)	(97.4, 77.9, 39.2)	(95.6, 82.1, 17.2)	(96.1, 89.1, 16.2)
metal_plate	(95.9, 85.3, 70.4)	(93.0, 74.5, 63.1)	(93.7, 86.8, 61.9)	(92.0, 33.5, 57.8)	(93.9, 83.4, 62.5)	(95.3, 89.3, 66.8)
tubes	(90.7, 69.7, 17.3)	(99.1, 96.9, 68.7)	(98.1, 93.6, 53.3)	(98.9, 90.4, 70.0)	(98.9, 95.7, 61.0)	(99.2, 97.1, 70.2)
Mean	(62.3, 38.3, 15.6)	(94.3, 83.8, 31.3)	(96.5, 88.7, 34.2)	(96.0, 62.8, 34.5)	(97.0, 89.3, 38.2)	(97.6, 93.2, 41.9)

Table 13. **Category-level anomaly classification performance for the dataset MPDD.** each triplet reports (AUROC, AP, F1-max).

Product	AnVoL	VAND	AnomalyCLIP	AdaCLIP	Crane w/o D-Attn	Crane
bracket_black	(42.5, 59.7, 76.5)	(68.4, 72.6, 80.0)	(67.8, 73.4, 78.6)	(71.4, 81.1, 77.7)	(82.1, 74.1, 66.7)	(83.3, 70.3, 71.8)
bracket_brown	(66.7, 92.3, 90.7)	(61.6, 78.0, 81.0)	(62.0, 80.4, 80.3)	(51.9, 71.8, 79.7)	(80.8, 81.8, 76.9)	(84.0, 82.7, 82.5)
bracket_white	(38.5, 58.2, 76.5)	(85.7, 88.2, 78.1)	(67.7, 71.6, 69.8)	(77.8, 80.0, 74.7)	(72.9, 77.7, 81.1)	(76.9, 81.8, 79.6)
connector	(100, 100, 100)	(78.5, 71.7, 66.7)	(87.4, 77.0, 73.7)	(64.4, 61.9, 58.3)	(64.9, 80.1, 81.0)	(54.6, 74.4, 79.7)
metal_plate	(98.3, 99.4, 95.9)	(69.9, 86.5, 86.6)	(84.7, 94.4, 87.5)	(86.6, 94.8, 90.3)	(91.4, 96.8, 90.9)	(89.9, 96.6, 89.7)
tubes	(90.4, 95.4, 90.4)	(95.7, 98.1, 92.2)	(95.4, 98.1, 92.3)	(80.8, 91.6, 84.7)	(96.4, 98.5, 93.0)	(97.5, 99.0, 94.8)
Mean	(72.7, 83.6, 88.3)	(76.6, 82.5, 80.8)	(77.5, 82.5, 80.4)	(72.1, 80.2, 77.6)	(81.4, 84.8, 81.6)	(81.0, 84.1, 83.0)

Table 14. **Category-level anomaly localization performance for the dataset MVTec-AD.** each triplet reports (AUROC, AUPRO, F1-max).

Product	AnVoL	VAND	AnomalyCLIP	AdaCLIP	Crane w/o D-Attn	Crane
bottle	(90.9, 75.7, 53.2)	(83.5, 45.6, 53.4)	(90.4, 80.8, 51.6)	(90.8, 57.6, 60.8)	(91.6, 84.6, 54.6)	(93.6, 88.2, 60.6)
grid	(67.7, 66.3, 23.0)	(72.3, 25.7, 23.9)	(78.9, 64.0, 18.9)	(78.3, 35.3, 26.5)	(97.7, 80.0, 35.7)	(99.2, 95.5, 48.1)
carpet	(82.8, 52.4, 14.9)	(92.0, 51.3, 33.1)	(95.8, 87.6, 31.0)	(95.2, 18.0, 32.9)	(99.0, 91.9, 59.2)	(99.3, 95.8, 66.8)
capsule	(95.6, 85.1, 42.5)	(98.4, 48.5, 65.7)	(98.8, 90.0, 57.0)	(98.9, 36.1, 67.4)	(96.0, 90.5, 33.8)	(95.5, 92.4, 33.5)
cable	(95.7, 87.1, 22.3)	(95.8, 31.6, 40.8)	(97.3, 75.4, 32.0)	(97.0, 20.3, 39.0)	(77.7, 68.8, 23.1)	(79.4, 71.5, 22.0)
hazelnut	(93.8, 75.6, 32.5)	(96.1, 70.2, 50.5)	(97.2, 92.5, 47.6)	(96.5, 59.2, 40.1)	(97.1, 94.3, 50.6)	(97.4, 94.8, 53.2)
leather	(98.7, 94.4, 36.3)	(99.1, 72.4, 50.0)	(98.6, 92.2, 33.2)	(99.3, 76.9, 47.7)	(99.1, 97.2, 40.7)	(99.1, 98.3, 41.4)
metal_nut	(71.4, 46.5, 29.6)	(65.5, 38.4, 28.0)	(74.6, 71.1, 33.1)	(74.4, 62.4, 35.3)	(72.7, 74.4, 33.4)	(76.9, 80.1, 34.0)
screw	(79.5, 69.8, 18.4)	(76.2, 65.4, 27.7)	(91.8, 88.1, 35.5)	(87.7, 27.9, 35.7)	(98.4, 91.7, 33.8)	(98.6, 92.8, 39.3)
pill	(88.5, 60.1, 13.5)	(97.8, 67.1, 41.7)	(97.5, 88.0, 33.4)	(98.3, 70.3, 34.5)	(89.1, 90.8, 28.7)	(85.1, 91.3, 27.5)
toothbrush	(77.0, 54.3, 35.9)	(92.7, 26.7, 66.5)	(94.7, 87.4, 64.9)	(91.1, 30.1, 61.9)	(93.5, 90.4, 35.8)	(89.7, 90.8, 29.5)
wood	(91.6, 80.1, 20.6)	(95.8, 54.5, 48.1)	(91.9, 88.5, 29.0)	(94.7, 69.4, 37.9)	(97.5, 93.8, 60.7)	(96.7, 96.0, 60.8)
transistor	(75.6, 50.9, 24.6)	(62.4, 21.3, 19.0)	(70.8, 58.2, 18.8)	(57.8, 31.2, 16.3)	(69.5, 56.0, 17.7)	(65.4, 54.8, 16.7)
tile	(95.1, 75.1, 49.7)	(95.8, 31.1, 60.3)	(96.4, 91.5, 55.2)	(92.6, 48.1, 56.0)	(96.1, 87.5, 65.7)	(95.5, 90.3, 68.0)
zipper	(94.3, 82.2, 35.1)	(91.1, 10.7, 40.5)	(91.3, 65.4, 45.0)	(95.8, 18.2, 57.2)	(95.1, 77.3, 46.3)	(97.3, 89.3, 54.9)
Mean	(86.6, 70.4, 30.1)	(87.6, 44.0, 43.3)	(91.1, 81.4, 39.1)	(89.9, 44.1, 43.4)	(91.3, 84.6, 41.3)	(91.2, 88.1, 43.8)

Table 15. **Category-level anomaly classification performance for the dataset MVTec-AD.** each triplet reports (AUROC, AP, F1-max).

Product	AnVoL	VAND	AnomalyCLIP	AdaCLIP	Crane w/o D-Attn	Crane
bottle	(96.3, 99.0, 96.8)	(91.8, 97.6, 92.1)	(88.7, 96.8, 90.9)	(97.8, 99.3, 95.4)	(91.3, 97.5, 91.1)	(92.4, 97.7, 92.8)
grid	(87.8, 92.0, 86.0)	(88.3, 93.0, 85.1)	(70.3, 81.7, 77.4)	(64.3, 79.2, 76.0)	(99.7, 99.9, 98.3)	(100 , 100 , 100)
carpet	(79.1, 94.5, 92.7)	(79.8, 95.4, 92.0)	(89.5, 97.8, 91.7)	(84.6, 96.6, 92.0)	(100 , 100 , 100)	(99.9, 100 , 99.4)
capsule	(99.3, 99.8, 99.4)	(99.5, 99.8, 98.3)	(100 , 100 , 99.4)	(100 , 100 , 100)	(93.5, 98.6, 94.1)	(92.3, 98.3, 93.8)
cable	(98.1, 99.4, 96.4)	(86.4, 95.0, 89.1)	(97.8, 99.3, 97.3)	(97.7, 99.1, 97.4)	(87.1, 92.5, 83.9)	(88.1, 93.4, 86.2)
hazelnut	(94.0, 96.9, 89.4)	(89.5, 94.7, 87.0)	(97.2, 98.5, 92.6)	(87.0, 93.0, 86.1)	(98.5, 99.3, 96.4)	(98.0, 99.1, 96.3)
leather	(100 , 100 , 100)	(99.7, 99.9, 98.9)	(99.8, 99.9, 99.5)	(99.9, 99.9, 99.5)	(100 , 100 , 100)	(100 , 100 , 100)
metal_nut	(97.4, 99.4, 96.7)	(68.5, 91.9, 89.4)	(92.4, 98.2, 93.7)	(66.6, 92.1, 89.4)	(79.9, 95.5, 90.3)	(84.1, 96.4, 89.9)
screw	(86.6, 97.2, 91.8)	(80.6, 96.0, 91.6)	(81.1, 95.3, 92.1)	(88.9, 97.6, 94.0)	(90.0, 95.8, 91.6)	(92.4, 97.3, 92.1)
pill	(78.0, 92.1, 87.1)	(84.7, 93.5, 88.8)	(82.1, 92.9, 88.3)	(88.1, 95.0, 90.0)	(84.8, 96.7, 93.5)	(87.0, 97.5, 92.2)
toothbrush	(100 , 100 , 99.4)	(99.9, 99.9, 98.8)	(100 , 100 , 100)	(100 , 100 , 100)	(95.8, 98.7, 95.1)	(86.4, 95.1, 88.5)
wood	(92.2, 96.9, 93.1)	(54.0, 72.2, 83.3)	(85.3, 93.9, 90.0)	(91.1, 97.0, 90.9)	(98.6, 99.6, 97.4)	(97.9, 99.4, 97.5)
transistor	(86.4, 86.5, 77.9)	(81.1, 77.6, 74.5)	(93.9, 92.1, 83.7)	(86.8, 87.4, 78.7)	(90.6, 88.6, 79.1)	(91.8, 90.2, 79.5)
tile	(99.3, 99.8, 98.3)	(99.0, 99.7, 96.8)	(96.9, 99.2, 96.6)	(99.0, 99.7, 96.7)	(99.7, 99.9, 98.8)	(99.7, 99.9, 98.8)
zipper	(92.9, 97.9, 93.3)	(89.5, 97.1, 90.8)	(98.4, 99.5, 97.9)	(99.3, 99.8, 98.3)	(97.6, 99.3, 97.9)	(99.0, 99.7, 97.5)
Mean	(92.5, 96.7, 93.2)	(86.2, 93.6, 90.4)	(91.6, 96.4, 92.7)	(90.1, 95.7, 92.3)	(93.8, 97.5, 93.8)	(93.9, 97.6, 93.6)

Table 16. **Category-level anomaly localization performance for the dataset ViSA.** each triplet reports (AUROC, AUPRO, F1-max).

Product	AnVoL	VAND	AnomalyCLIP	AdaCLIP	Crane w/o D-Attn	Crane
candle	(95.6, 83.4, 14.7)	(97.8, 92.5, 39.4)	(98.8, 96.5, 75.6)	(99.2, 76.7, 48.2)	(86.2, 92.2, 16.7)	(90.4, 94.9, 13.5)
capsules	(82.9, 44.4, 9.8)	(97.5, 86.7, 48.5)	(95.0, 78.9, 82.2)	(98.7, 76.1, 47.6)	(99.0, 87.3, 67.1)	(95.7, 89.3, 32.6)
cashew	(89.8, 85.7, 11.1)	(86.0, 91.7, 22.9)	(93.8, 91.9, 80.3)	(95.9, 49.3, 34.2)	(96.8, 88.4, 43.4)	(99.4, 93.7, 69.6)
chewinggum	(91.4, 56.0, 49.3)	(99.5, 87.2, 78.5)	(99.3, 90.9, 94.8)	(99.5, 64.9, 79.5)	(94.8, 84.7, 33.7)	(93.8, 90.7, 27.3)
fryum	(77.9, 56.4, 23.8)	(92.0, 89.7, 29.7)	(94.6, 86.9, 90.1)	(94.1, 69.2, 28.9)	(98.5, 92.3, 37.6)	(98.9, 97.5, 40.3)
macaroni1	(81.9, 41.0, 1.1)	(98.8, 93.2, 35.5)	(98.3, 89.8, 80.4)	(99.7, 82.8, 35.0)	(92.0, 86.8, 15.7)	(93.3, 89.5, 17.5)
macaroni2	(78.0, 34.4, 0.1)	(97.8, 82.3, 13.7)	(97.6, 84.0, 71.2)	(99.0, 72.1, 14.2)	(93.7, 81.2, 22.3)	(93.9, 83.7, 25.0)
pcb1	(91.1, 72.1, 17.9)	(92.7, 87.5, 12.5)	(94.0, 80.7, 78.8)	(92.5, 59.0, 23.8)	(89.8, 79.5, 15.6)	(88.4, 79.6, 16.1)
pcb2	(85.1, 54.4, 3.0)	(89.7, 75.5, 23.4)	(92.4, 78.9, 67.8)	(92.3, 78.8, 30.6)	(98.9, 90.0, 29.2)	(98.0, 86.0, 7.4)
pcb3	(76.0, 32.8, 1.2)	(88.4, 77.8, 21.7)	(88.4, 76.8, 66.4)	(87.9, 77.3, 33.7)	(98.3, 86.0, 07.3)	(99.2, 93.0, 34.2)
pcb4	(93.3, 78.4, 33.0)	(94.6, 86.8, 31.3)	(95.7, 89.4, 87.8)	(96.3, 87.5, 43.6)	(98.0, 91.5, 43.2)	(97.4, 97.4, 37.8)
pipe_fryum	(79.2, 87.5, 10.8)	(96.0, 90.9, 30.4)	(98.2, 96.2, 89.8)	(97.4, 81.7, 36.0)	(94.9, 90.0, 39.2)	(95.2, 91.6, 40.9)
Mean	(85.2, 60.5, 14.6)	(94.2, 86.8, 32.3)	(95.5, 86.7, 28.3)	(96.0, 72.9, 37.9)	(95.1, 87.5, 30.9)	(95.3, 90.6, 30.2)

Table 17. **Category-level anomaly classification performance for the dataset ViSA.** each triplet reports (AUROC, AP, F1-max).

Product	AnVoL	VAND	AnomalyCLIP	AdaCLIP	Crane w/o D-Attn	Crane
candle	(97.2, 97.2, 92.5)	(83.5, 86.6, 77.1)	(80.9, 82.6, 37.8)	(94.5, 95.8, 89.1)	(83.3, 92.9, 82.2)	(85.9, 93.7, 84.5)
capsules	(80.6, 89.4, 80.5)	(61.4, 74.5, 78.0)	(82.8, 89.4, 37.8)	(74.3, 82.1, 80.9)	(97.5, 99.0, 96.9)	(81.5, 90.0, 80.2)
cashew	(90.2, 95.7, 86.8)	(86.9, 94.0, 84.8)	(76.0, 89.3, 25.8)	(93.7, 97.3, 92.2)	(84.4, 91.2, 83.7)	(97.9, 99.2, 96.4)
chewinggum	(96.7, 98.6, 94.8)	(96.5, 98.4, 93.7)	(97.2, 98.8, 61.0)	(91.6, 96.5, 89.6)	(95.1, 97.8, 92.3)	(92.7, 96.8, 90.2)
fryum	(90.2, 95.6, 88.7)	(94.2, 97.2, 91.7)	(92.7, 96.6, 30.3)	(86.1, 93.5, 84.7)	(87.1, 89.9, 80.0)	(83.5, 87.2, 76.4)
macaroni1	(70.4, 70.8, 71.4)	(71.4, 70.4, 71.7)	(86.7, 85.5, 23.7)	(73.2, 66.1, 75.7)	(83.6, 84.9, 79.3)	(83.5, 85.5, 77.0)
macaroni2	(61.7, 61.2, 68.9)	(64.7, 63.3, 69.1)	(72.2, 70.8, 5.1)	(53.9, 52.8, 68.3)	(74.0, 75.0, 72.5)	(74.7, 76.5, 72.5)
pcb1	(79.7, 82.4, 75.6)	(53.8, 57.4, 66.9)	(85.2, 86.7, 12.7)	(59.7, 64.1, 67.1)	(68.2, 73.0, 66.4)	(57.1, 65.1, 66.4)
pcb2	(56.2, 53.9, 68.1)	(71.6, 73.8, 70.0)	(62.0, 64.4, 15.8)	(53.1, 56.6, 66.7)	(85.4, 87.1, 77.6)	(68.5, 66.4, 69.9)
pcb3	(66.4, 68.2, 69.0)	(66.9, 70.8, 66.7)	(61.7, 69.4, 9.3)	(65.4, 69.8, 66.9)	(69.1, 68.3, 71.0)	(85.7, 86.5, 77.2)
pcb4	(75.9, 75.7, 73.6)	(95.1, 95.2, 87.3)	(93.9, 94.3, 34.7)	(77.4, 79.9, 74.6)	(98.7, 99.4, 96.0)	(97.0, 98.5, 94.0)
pipe_fryum	(85.4, 92.9, 85.5)	(89.7, 94.7, 87.8)	(92.3, 96.3, 45.5)	(85.9, 92.8, 86.1)	(97.0, 96.8, 93.1)	(94.9, 94.5, 89.2)
Mean	(79.2, 81.6, 79.6)	(78.0, 81.4, 78.7)	(82.0, 85.3, 80.4)	(75.7, 79.0, 78.5)	(85.3, 87.9, 82.6)	(83.6, 86.6, 81.2)

D.2 Category-level Qualitative Results

To provide visual intuition of `Crane`'s capability in capturing anomalous patterns, we present zero-shot anomaly maps across diverse domains, objects, and textures. For MVTEC-AD, we visualize results for the products capsule, carpet, grid, hazelnut, toothbrush, tile, and zipper. For ViSA, we illustrate anomaly maps for the categories candles, capsules, cashew, and pipe_fryum. Localization predictions for the anomalous classes `white_brackets`, `tubes`, and `plates` are reported for MPDD. In DTD-Synthetic, we provide visualizations for the Matted and Fibrous classes, while for DAGM, we include `class06`, `class07`, `class08`, and `class09`. Additionally, results for the single class from the KSDD dataset are presented. For medical anomaly detection, we provide zero-shot localization outputs for BrainMRI, ISIC, and CVC-ColonDB, using the medical training scheme discussed earlier at Appendix C.



Figure 4. Localization score maps for the product, capsule, in MVTec-AD. The first row illustrates the original image, while the second row shows the anomaly segmentation results, with the regions encircled in green representing the ground truth.

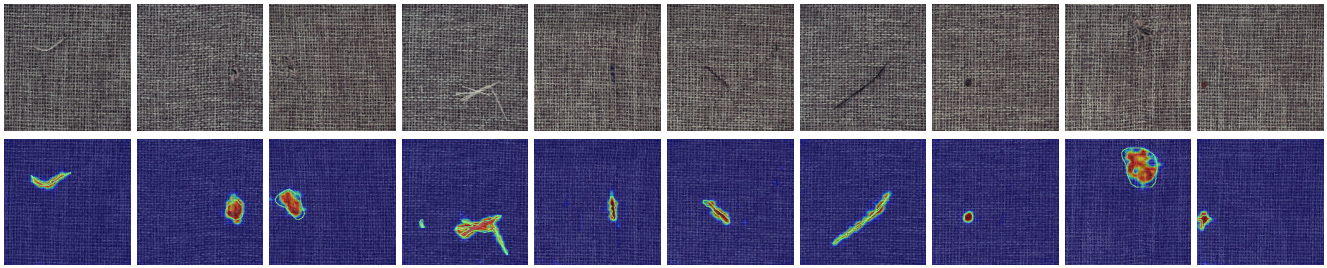


Figure 5. Localization score maps for the product, carpet, in MVTec-AD. The first row illustrates the original image, while the second row shows the anomaly segmentation results, with the regions encircled in green representing the ground truth.

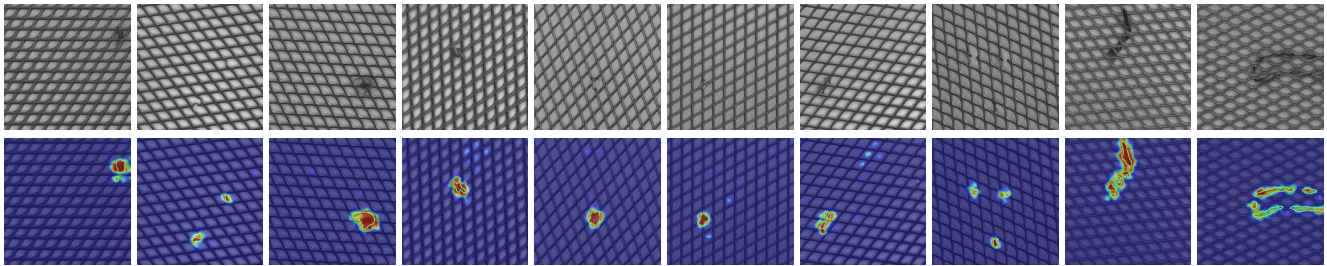


Figure 6. Localization score maps for the product, grid, in MVTec-AD. The first row illustrates the original image, while the second row shows the anomaly segmentation results, with the regions encircled in green representing the ground truth.

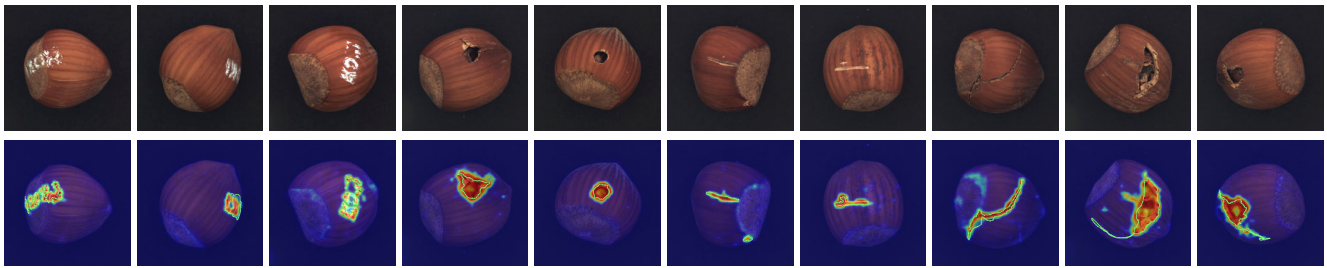


Figure 7. Localization score maps for the product, hazelnut, in MVTec-AD. The first row illustrates the original image, while the second row shows the anomaly segmentation results, with the regions encircled in green representing the ground truth.

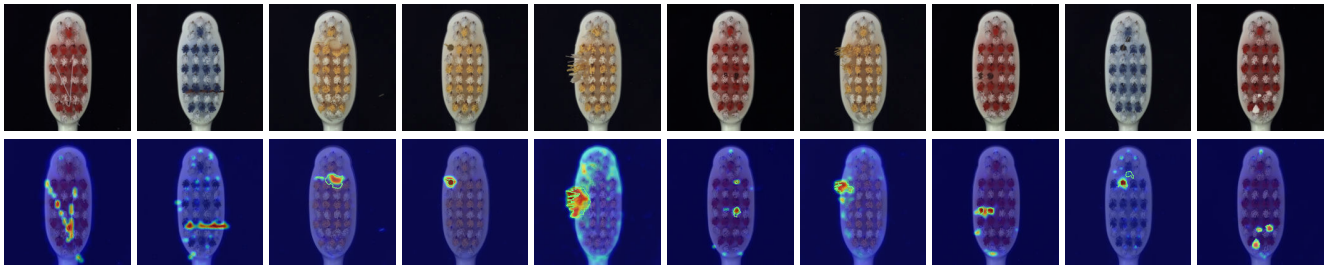


Figure 8. Localization score maps for the product, toothbrush, in MVTec-AD. The first row illustrates the original image, while the second row shows the anomaly segmentation results, with the regions encircled in green representing the ground truth.

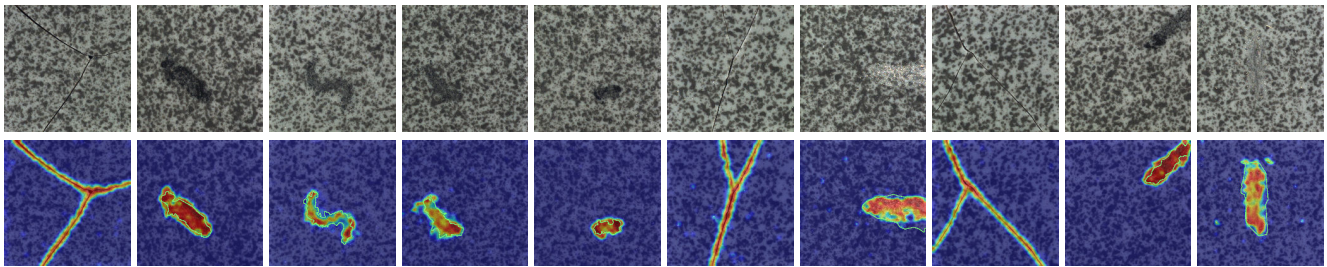


Figure 9. Localization score maps for the product, tile, in MVTec-AD. The first row illustrates the original image, while the second row shows the anomaly segmentation results, with the regions encircled in green representing the ground truth.

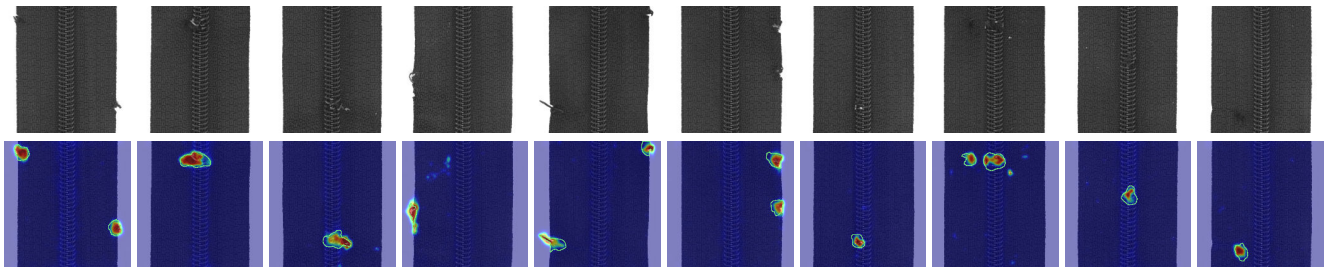


Figure 10. Localization score maps for the product, zipper, in MVTec-AD. The first row illustrates the original image, while the second row shows the anomaly segmentation results, with the regions encircled in green representing the ground truth.

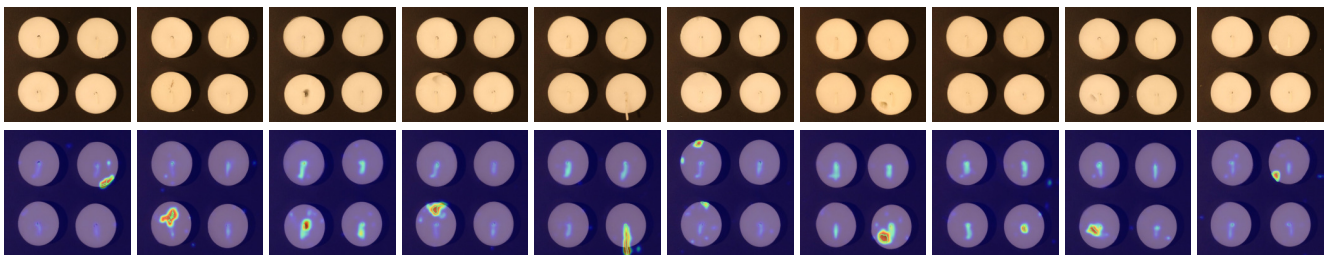


Figure 11. Localization score maps for the product, candles, in VISA dataset. The first row illustrates the original image, while the second row shows the anomaly segmentation results, with the regions encircled in green representing the ground truth.

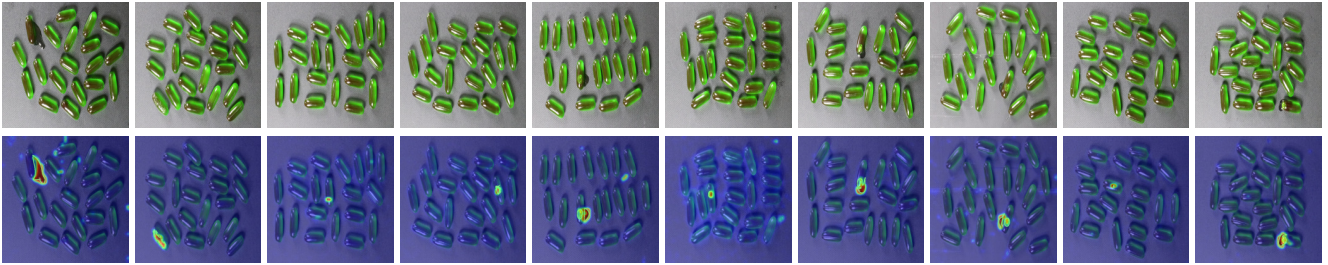


Figure 12. Localization score maps for the product, capsules, in VISA dataset. The first row illustrates the original image, while the second row shows the anomaly segmentation results, with the regions encircled in green representing the ground truth.

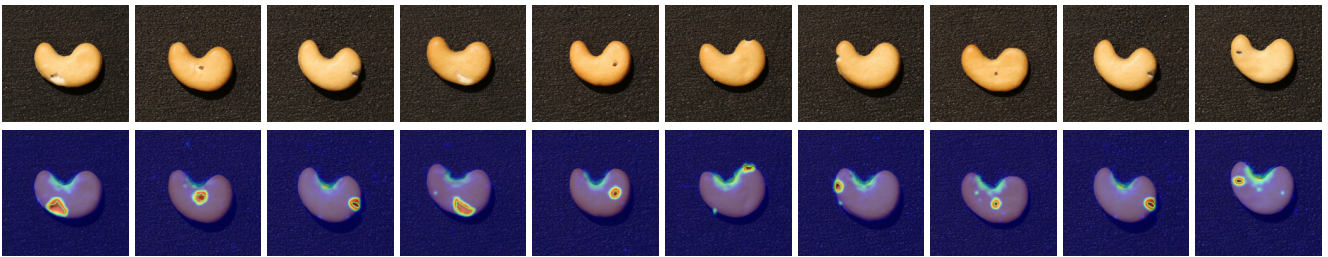


Figure 13. Localization score maps for the product, cashew, in VISA dataset. The first row illustrates the original image, while the second row shows the anomaly segmentation results, with the regions encircled in green representing the ground truth.

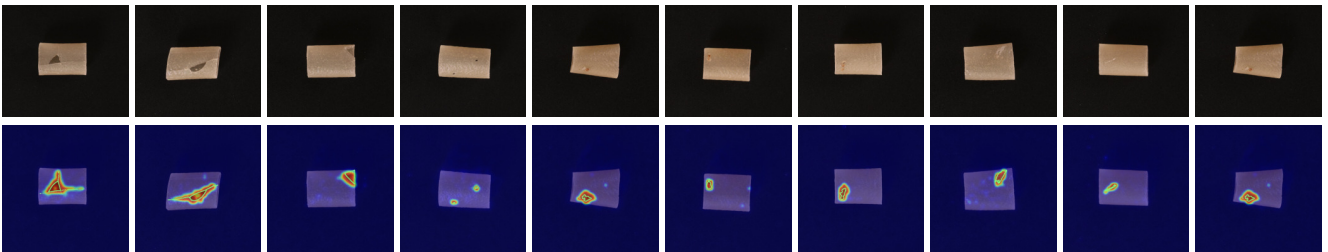


Figure 14. Localization score maps for the product, pipe fryum, in VISA dataset. The first row illustrates the original image, while the second row shows the anomaly segmentation results, with the regions encircled in green representing the ground truth.

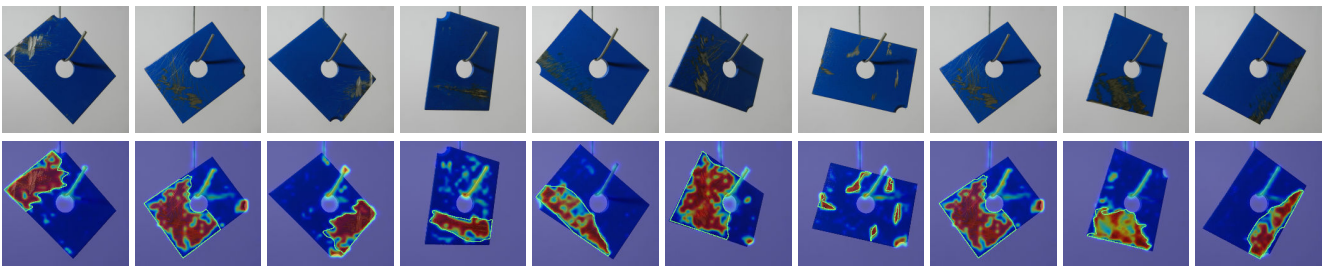


Figure 15. Localization score maps for the product, plates, in MPDD dataset. The first row illustrates the original image, while the second row shows the anomaly segmentation results, with the regions encircled in green representing the ground truth.

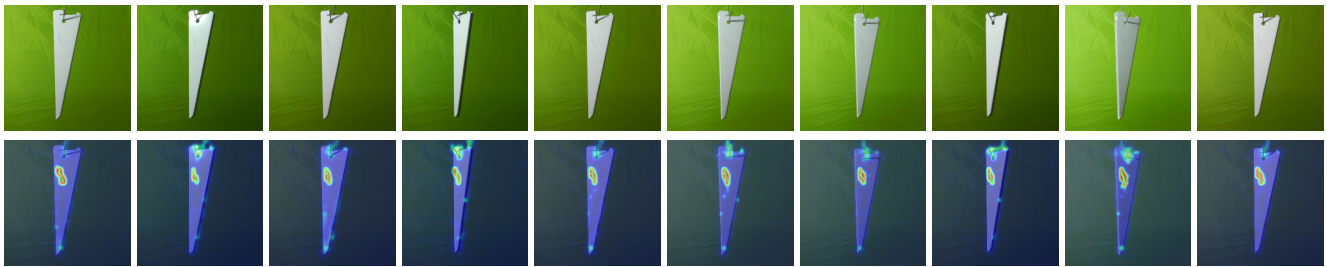


Figure 16. Localization score maps for the product, white brackets, in MPDD dataset. The first row illustrates the original image, while the second row shows the anomaly segmentation results, with the regions encircled in green representing the ground truth.

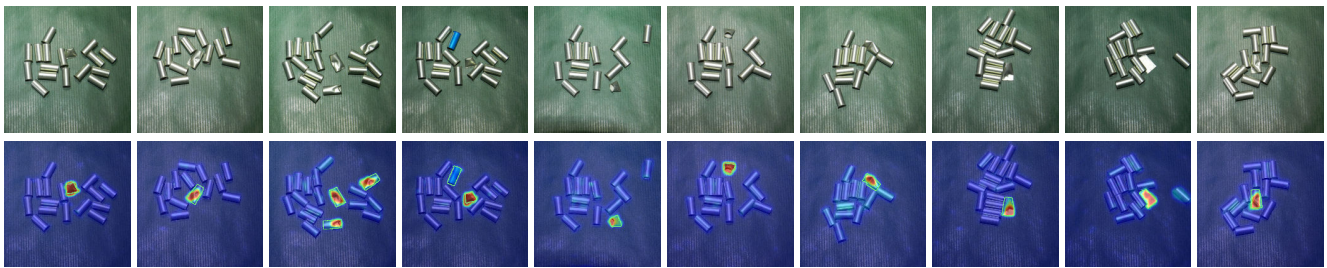


Figure 17. Localization score maps for the product, tubes, in MPDD dataset. The first row illustrates the original image, while the second row shows the anomaly segmentation results, with the regions encircled in green representing the ground truth.

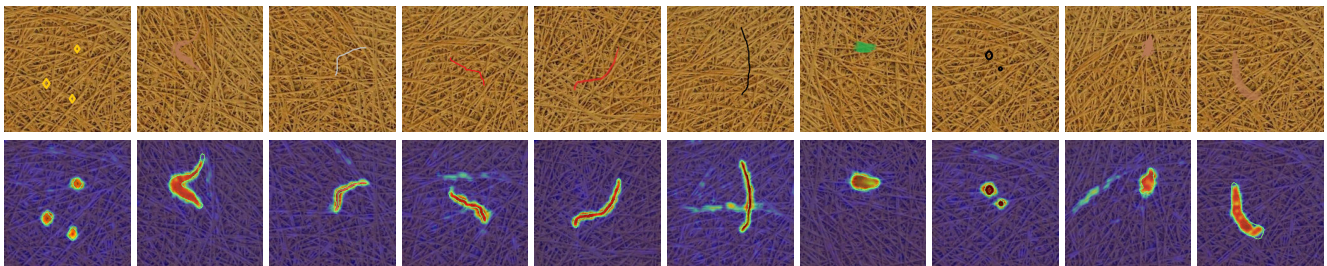


Figure 18. Localization score maps for the product, fibrous, in DTD dataset. The first row illustrates the original image, while the second row shows the anomaly segmentation results, with the regions encircled in green representing the ground truth.

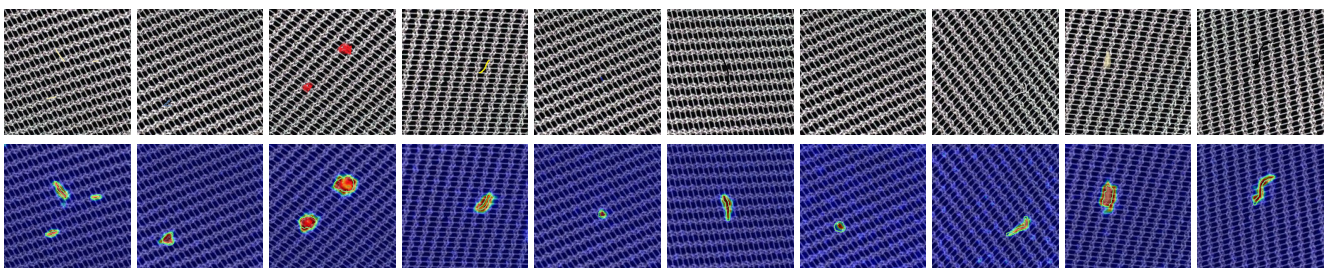


Figure 19. Localization score maps for the product, matted, in DTD dataset. The first row illustrates the original image, while the second row shows the anomaly segmentation results, with the regions encircled in green representing the ground truth.

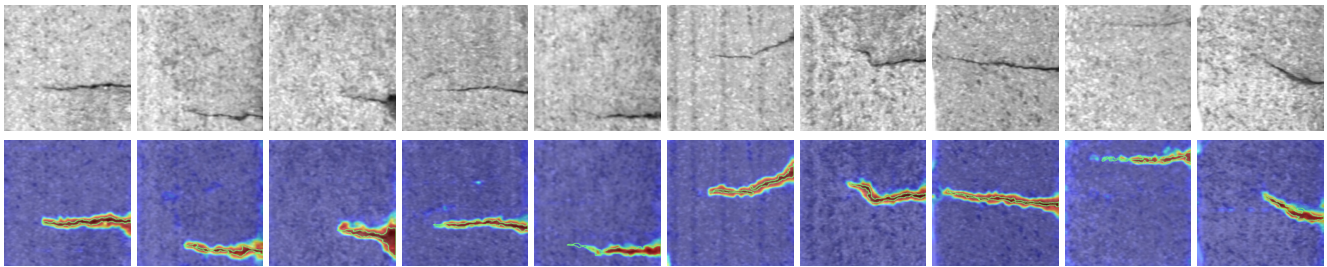


Figure 20. Localization score maps for the product, electric commutators, in SDD dataset. The first row illustrates the original image, while the second row shows the anomaly segmentation results, with the regions encircled in green representing the ground truth.

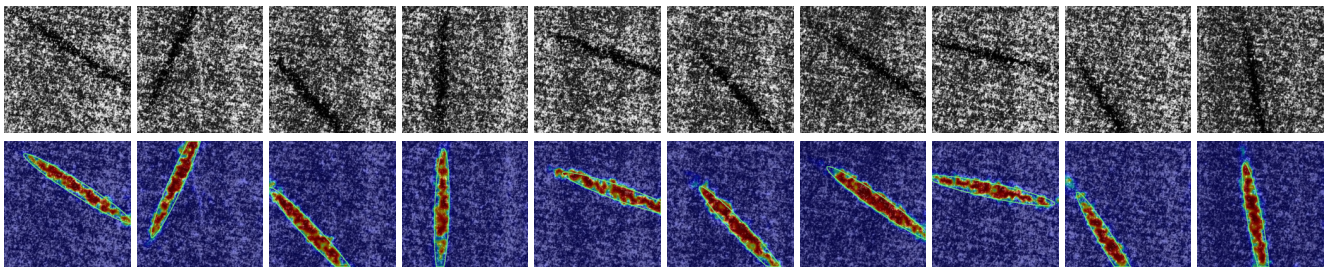


Figure 21. Localization score maps for the product, class 06, in DAGM dataset. The first row illustrates the original image, while the second row shows the anomaly segmentation results, with the regions encircled in green representing the ground truth.

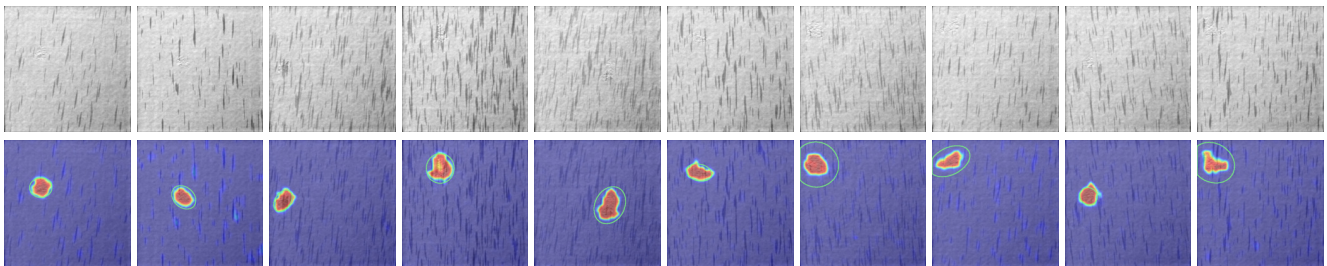


Figure 22. Localization score maps for the product, class 7, in DAGM dataset. The first row illustrates the original image, while the second row shows the anomaly segmentation results, with the regions encircled in green representing the ground truth.

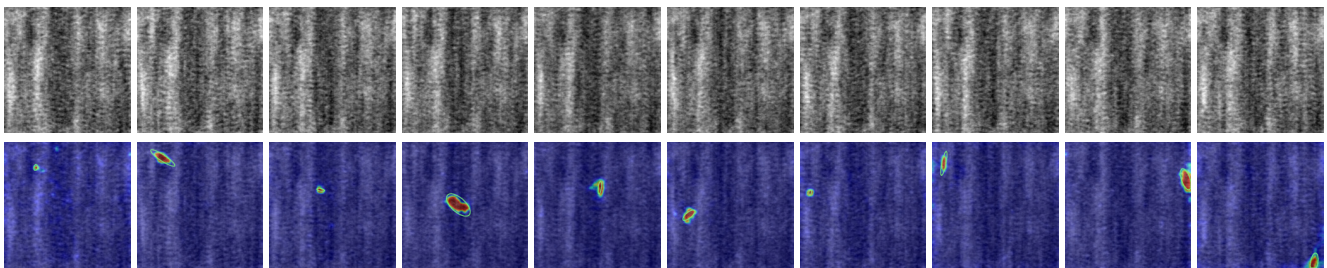


Figure 23. Localization score maps for the product, class 08, in DAGM dataset. The first row illustrates the original image, while the second row shows the anomaly segmentation results, with the regions encircled in green representing the ground truth.

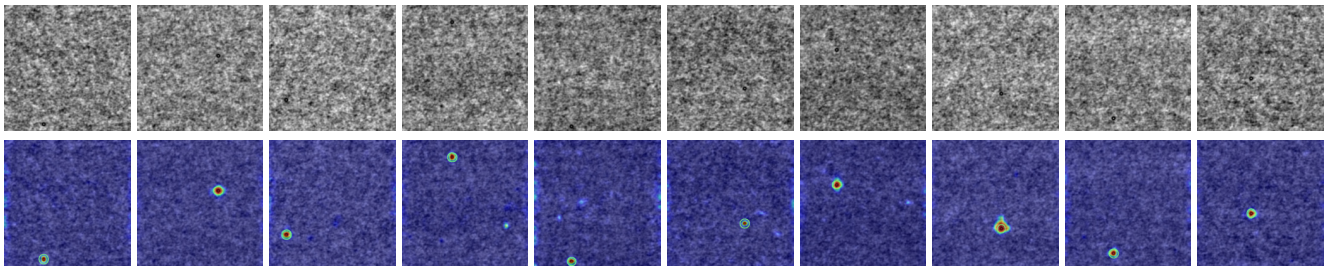


Figure 24. Localization score maps for the product, class 09, in DAGM dataset. The first row illustrates the original image, while the second row shows the anomaly segmentation results, with the regions encircled in green representing the ground truth.

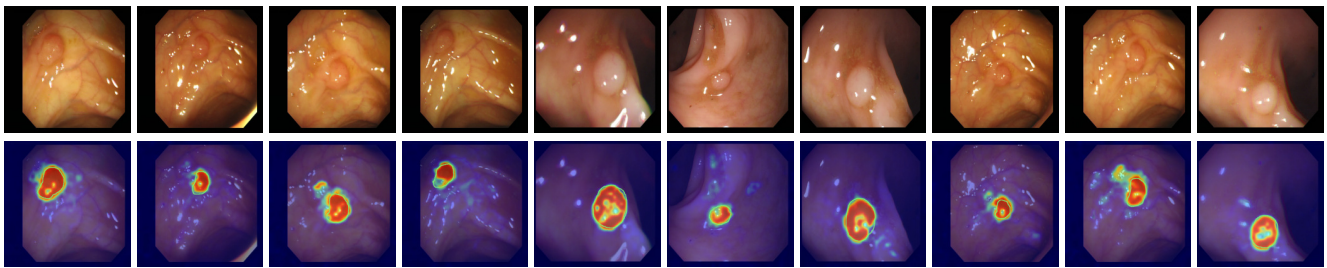


Figure 25. Localization score maps for the ColonDB dataset. The first row illustrates the original image, while the second row shows the anomaly segmentation results, with the regions encircled in green representing the ground truth.

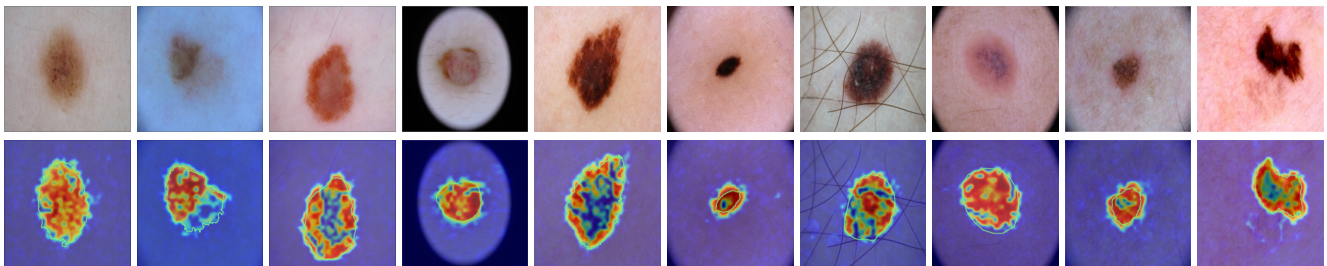


Figure 26. Localization score maps for the ICIC dataset. The first row illustrates the original image, while the second row shows the anomaly segmentation results, with the regions encircled in green representing the ground truth.

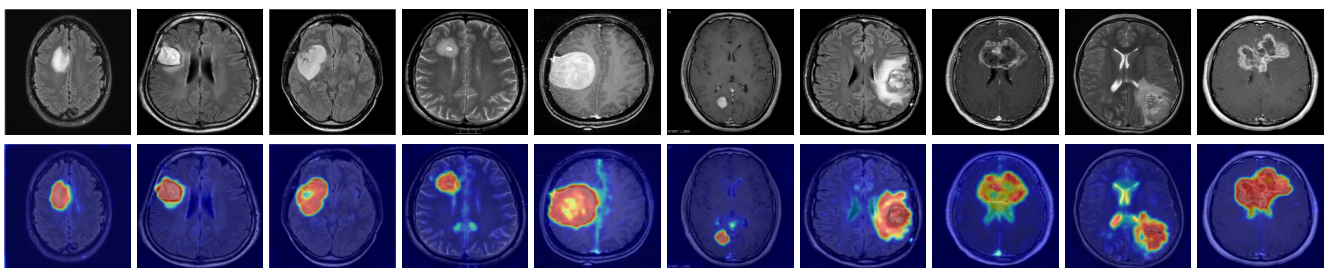


Figure 27. Localization score maps for the BrainMRI dataset. The first row illustrates the original image, while the second row shows the anomaly segmentation results, with the regions encircled in green representing the ground truth.